Widespread Exposures of Extensive Clean Shallow Ice in the Mid-Latitudes of Mars

Colin M Dundas, Michael T Mellon, Susan J. Conway, Ingrid J Daubar, Kaj E Williams, Lujendra Ojha, James J Wray, Ali M Bramson, Shane Byrne, Alfred S Mcewen, et al.

1   **Widespread Exposures of Extensive Clean Shallow Ice in the Mid-Latitudes of Mars**

2

3   Colin M. Dundas[a] *

4   Michael T. Mellon[b]

5   Susan J. Conway[c]

6   Ingrid J. Daubar[d]

7   Kaj E. Williams[a]

8   Lujendra Ojha[e]

9   James J. Wray[f]

10   Ali M. Bramson[g]

11   Shane Byrne[h]

12   Alfred S. McEwen[h]

13   Liliya V. Posiolova[i]

14   Gunnar Speth[i]

15   Donna Viola[j]

16   Margaret E. Landis[k]

17   Gareth A. Morgan[l]

18   Asmin V. Pathare[l]

19

20   [a]U.S. Geological Survey, Astrogeology Science Center, 2255 N. Gemini Dr., Flagstaff,

21   AZ 86001, USA (cdundas@usgs.gov).

22   [b]Center for Astrophysics and Planetary Science, Cornell University, Ithaca, NY, USA.

23 [c]Laboratoire de Planétologie et Géodynamique CNRS UMR 6112, Université de Nantes,

24 France.

25 [d]Department of Earth, Environmental, and Planetary Sciences, Brown University,

26 Providence, RI, USA.

27 [e]Department of Earth and Planetary Sciences, Rutgers University, Piscataway, NJ, USA.

28 [f]School of Earth and Atmospheric Sciences, Georgia Institute of Technology, Atlanta,

29 GA, USA.

30 [g]Department of Earth, Atmospheric, and Planetary Sciences, Purdue University, West

31 Lafayette, IN, USA.

32 [h]Lunar and Planetary Laboratory, The University of Arizona, Tucson, AZ, USA.

33 [i]Malin Space Science Systems, San Diego, CA, USA.

34 [j]NASA Ames Research Center, Moffett Field, CA, USA.

35 [k]Laboratory for Atmospheric and Space Physics, University of Colorado, Boulder, CO,

36 USA.

37 [l]Planetary Science Institute, Tucson, AZ, USA.

38

39 *Corresponding author.

40
41

42

43

Abstract

Although ice in the Martian mid-latitudes is typically covered by a layer of dust or regolith, it is exposed in some locations by fresh impact craters or in erosional scarps. In both cases, the exposed ice is massive or excess ice with a low lithic content. We find that erosional scarps occur between 50–61° north and south latitude and that they are concentrated in and near Milankovič crater in the northern hemisphere and southeast of the Hellas basin in the southern hemisphere. These may represent locations of particularly thick or clean bodies of ice. Pits created by retreat of the scarps represent sublimation-thermokarst landforms that evolve in a manner distinct from other ice-loss landforms on Mars. New impact craters reveal that clean subsurface ice is widespread at middle and high latitudes in both hemispheres at depths less than 1 meter. Both the depth to ice and the ice content appear to exhibit significant variability over tens to hundreds of meters. The lowest-latitude exposed ice is near 39 °N and is at the edge of a region where impact exposures between 40–50 °N are common, consistent with other indications of a high ice content. This lowest-latitude ice may be currently unstable and subliming. Impact craters on lineated valley fill excavate ice blocks that may represent the top of debris-covered glacial ice. Together, these landforms indicate widespread, clean subsurface ice at middle latitudes on Mars. The distribution and properties of this ice could provide information about past climate conditions.

Plain Language Summary

Ice occurs at the surface near the north and south poles of Mars, but in the mid-latitudes it is usually buried beneath rocks and dust. Impact craters and erosion expose

67   the ice in some places. At these locations, the ice is generally clean, with little dust or

68   rocky material embedded within it, in contrast with pore ice filling in voids in soil. The

69   erosional exposures are concentrated in and near Milankovič crater in the northern

70   hemisphere and southeast of the Hellas basin in the southern hemisphere and occur at a

71   narrow range of latitudes. These may be locations of particularly thick, clean ice. Impact

72   craters reveal that some amount of such subsurface ice is widespread. The craters help to

73   define the lowest latitude where ice is present and how deeply it is buried, which could

74   provide information about the history of the climate on Mars.

75

1. Introduction

One of the key needs identified by the Mars science community is the inventory and characterization of non-polar near-surface ice (Smith et al., 2018; MEPAG ICE-SAG Report, 2019). This is a fundamental question for determining the near-surface H_2O abundance on Mars and the processes by which it is transported, deposited, and modified. Theory indicates that ice stability is controlled by temperature and the atmospheric water vapor content (e.g., Leighton and Murray, 1966; Mellon and Jakosky, 1993; 1995; Mellon et al., 2004; Schorghofer and Aharonson, 2005; Chamberlain and Boynton, 2007; Steele et al., 2017), and thus a stability boundary varies over time depending on the history of those parameters. This climatic change in turn is governed by variations in Mars' orbit and obliquity (e.g., Murray et al., 1973; Ward, 1973; Laskar et al., 2004). Small adjustments of the ice-table depth in response to climate changes can occur within hundreds of years even in the presence of salt crusts or other plausible diffusion barriers (e.g., Mellon et al., 2004; Hudson and Aharonson, 2008). However, thick bodies of ice might survive through intervals of instability (e.g., Schorghofer and Forget, 2012; Bramson et al., 2017). There is evidence that shallow (<10 m) mid-latitude ice has survived for tens of millions of years (Viola et al., 2015) and debris-covered glaciers have an estimated mean age of 110 Ma since the last major ice accumulation (Fassett et al., 2014). Thus the distribution of ice is influenced by its stability in the geologically recent past as well as the present. Additionally, early expectations were that most subsurface ice would simply fill in the pore space of the regolith (e.g., Squyres and Carr, 1986; Mellon and Jakosky, 1993). However, many lines of evidence (e.g., Boynton et al., 2002; Mellon et al., 2009; Smith et al., 2009; Mouginot et al., 2010; Conway and Balme, 2014;

99   Bramson et al., 2015; Dundas et al., 2015; Stuurman et al., 2016; Pathare et al., 2018)

100   now point to the widespread occurrence of excess or massive ice (terminology per van

101   Everdingen (1998)) rather than pore ice, requiring additional processes such as snowfall

102   (e.g., Madeleine et al., 2009; 2014), thermal cycling to enhance porosity (Fisher, 2005),

103   or migration of thin liquid films to generate ice lenses (e.g., Sizemore et al., 2015).

104   Hence, assessing the distribution, concentration, and structure of ground ice is vital for

105   understanding recent Martian climate and its variations.

106   Ground ice in the Martian mid-latitudes is widespread, but almost always

107   underneath a desiccated protective layer of dry permafrost. This structure was first

108   predicted by Leighton and Murray (1966) and subsequently confirmed by refined models

109   (e.g., Mellon et al., 2004; Schorghofer and Aharonson, 2005; Chamberlain and Boynton,

110   2007; Steele et al., 2017). Observations from gamma-ray and neutron spectroscopy (e.g.,

111   Boynton et al., 2002; Mitrofanov et al., 2018; Pathare et al., 2018), thermal emission

112   (e.g., Bandfield, 2007; Bandfield and Feldman, 2008; Piqueux et al., 2019), and direct

113   excavation by the Phoenix lander (Mellon et al., 2009; Smith et al., 2009) confirm this

114   structure. Unfortunately, the desiccated layer shields the ice from direct view, and

115   exposed ice is expected to sublimate rapidly at mid-latitudes and create a new covering

116   deposit, so the ice is usually concealed beneath dust and regolith.

117   Natural exposures provide local information about the current state of subsurface

118   ice, such as the ice content, geographic distribution, and layering at each site. There are

119   two main categories of natural exposure. Small craters (Fig. 1a) pierce the desiccated

120   cover and create temporary exposures or excavate formerly buried ice onto their ejecta

121   blankets (Byrne et al., 2009; Dundas et al., 2014). These constitute high-resolution point

122   samples of the ice table and provide a valuable data set for comparison with less-direct,

123   lower-resolution approaches to understanding the distribution of ice. However, these

124   craters are small and shallow features, and the impact events also modify the ice relative

125   to its baseline state. Direct, high-resolution vertical information on undisturbed mid-

126   latitude ice structure was minimal until the discovery of scarp exposures (Fig. 1b) cutting

127   through the ice (Dundas et al., 2018). The scarps are kilometers long, tens of meters high,

128   and expose cross sections through the ice, revealing layering and unconformities. This ice

129   was interpreted as sintered snow with a very low lithic content, and indications of glacial

130   flow exist at one location. Rocks (>50 cm diameter) fell out of one of the scarps over

131   three Mars years, suggesting ongoing sublimation, which was also indicated by

132   weakening of H_2O spectral absorption features over the course of the summer (Dundas et

133   al., 2018). In addition to the scarps and craters, exposed ice has been reported in some

134   gully alcoves where it may be exposed by active erosion (Dundas et al., 2019; Khuller

135   and Christensen, 2019), but this process has not been studied in depth.

136   The scarps are incised in surface-mantling deposits. Latitude-dependent mantle

137   deposits were first observed by Mariner 9 (Soderblom et al., 1973). They were initially

138   thought to be aeolian dust deposits, but higher-resolution imaging provided evidence that

139   they contain ice (Mustard et al., 2001), in some cases forming thick units with a high ice

140   content (Conway and Balme, 2014). Layering indicates deposition in multiple distinct

141   episodes (Schon et al., 2009). Polygonal cracking visible in some of these units (e.g.,

142   Mangold, 2005; Levy et al., 2009a) indicates a structural integrity that is best interpreted

143   as thermal contraction cracking of solid ice or ice-cemented regolith. These surface-

144   mantling deposits are now widely thought to have been deposited as mixtures of snow or

145 frost and dust (in unknown and probably variable proportions) within the last few million

146 years during periods when Mars' axial tilt was higher than at present (e.g., Mustard et al.,

147 2001; Head et al., 2003; Schon et al., 2009; Madeleine et al., 2014).

148   Dundas et al. (2018) documented seven scarp exposure sites in the southern

149 hemisphere and one cluster in Milankovič crater in the north; Harish et al. (2020)

150 reported two additional scarps in the northern hemisphere. However, neither conducted a

151 comprehensive survey. Additionally, the number of known ice-exposing craters has more

152 than doubled since publication of Dundas et al. (2014). This work reports an assessment

153 of the locations and properties of ice-exposing scarps in current data in both the northern

154 and southern mid-latitudes and reports on the expanded data set of icy craters.

155

156 **2. Methods**

157 *2.1. Data*

158   The data sets used for this work included Thermal Emission Imaging System

159 (THEMIS; Christensen et al., 2004) Daytime Infrared mosaics, Context Camera (CTX;

160 Malin et al., 2007) images, and High Resolution Imaging Science Experiment (HiRISE;

161 McEwen et al., 2007) images. The THEMIS products use daytime infrared observations

162 and provide near-global mosaics at 100 m/pix (Fergason et al., 2019). CTX images have

163 near-global coverage at 6 m/pix. HiRISE images reprojected to 25 or 50 cm/pix cover

164 only a small fraction of the surface and include a central swath with two additional colors

165 (from blue-green and near-infrared filters) within the wider red-filter image. These

166 images were often targeted to center on the features studied here. We used HiRISE data

167 through Mars Reconnaissance Orbiter orbit 64,199 for study of icy craters and through

168   orbit 66899 for icy scarps. We also inspected data from the Compact Reconnaissance

169   Imaging Spectrometer for Mars (CRISM; Murchie et al., 2007) where available. CRISM

170   is a visible and near-infrared spectrometer, which can provide more definitive evidence

171   for water ice than our other data sets, but observations are spatially limited and often do

172   not include the near-infrared wavelengths that provide the strongest evidence for ice. We

173   followed the same CRISM processing techniques used in Dundas et al. (2018).

174   Most HiRISE images include a near-infrared channel, so they do not detect the

175   same wavelengths as the human eye. Thus when displayed in color, they do not show true

176   colors. In the enhanced-color images shown in the figures herein (which are from

177   standard Reduced Data Records), the near-infrared filter data are displayed as red, the red

178   filter data are displayed as green, and the blue-green filter data are displayed as blue, and

179   the images are stretched to show local contrast and emphasize color variations; this is

180   standard procedure for HiRISE color products (Delamere et al., 2010). The stretch is

181   scene dependent for each observation, so conclusions about the apparent color of features

182   in different images depend on the scene having a similar range of colors and shadows.

183   This is often roughly true on Mars, where surface dust tends to be uniformly reddish.

184   However, differences in topography, atmospheric dust content, illumination, and

185   sublimation of ice can produce apparent differences in color between images as well as

186   color changes in unchanged parts of the surface when comparing images of the same site.

187   Both raw HiRISE data and calibrated top-of-atmosphere reflectance for each channel are

188   available via the Planetary Data System.

189   Materials that appear blue in stretched images may have a reddish true color but

190   are brighter than their surroundings in the HiRISE blue-green channel. Material that

191 appears white is brighter in all three channels, but generally not white in true color. We

192 refer to these enhanced colors as "relatively blue" or "relatively white" in the text below.

193 Relatively blue or relatively white coloration is not diagnostic of exposed ice (notably,

194 mafic materials including basaltic sand also appear relatively blue (Keszthelyi et al.,

195 2008; Delamere et al., 2010)). However, we considered the combination of a relatively

196 blue or relatively white color closely associated with the distinctive morphology of a

197 scarp or new crater sufficient to classify a feature as an ice exposure with a high degree

198 of confidence. Changes over time often support the presence of ice, as described below.

199

200 *2.2. Ice-Exposing Scarps*

201 We conducted a survey of the distribution of ice-exposing scarps with the

202 properties described by Dundas et al. (2018). We searched the THEMIS Daytime Infrared

203 controlled mosaics (Fergason et al., 2019) at latitudes equatorward of 65 °N/S and the

204 uncontrolled global mosaic version 12.0 (e.g., Edwards et al., 2011) poleward of 65 °N/S.

205 In the southern hemisphere, we searched latitudes 45–70 °S (planetocentric), and

206 observed scarps only between 50–61 °S. Based on the results of this search, we limited

207 the northern-hemisphere survey to 45–65 °N. All scarps identified in the northern

208 hemisphere were between 53–59 °N, indicating that these bounds were sufficiently wide.

209 Further support for these bounds is provided by Vincendon et al. (2010), who searched

210 CRISM data and found no exposed perennial ground ice between 45 °S and 50 °N. We

211 looked for irregular pits greater than a few hundred meters across and checked candidates

212 using images from CTX to look for the main identifying characteristic of ice-exposing

213 scarps: an approximately straight, smooth, sharp-edged, pole-facing scarp (Fig. 1b).

214   Candidates possessing such a scarp were classified as probable if no HiRISE color data

215   were available or considered confirmed if they displayed a distinct relatively blue

216   coloration in HiRISE images. In some of the cases from Dundas et al. (2018), spectral

217   evidence provides additional confirmation of water ice, but CRISM data are often not

218   available. An additional requirement was that coloration was present in late spring or

219   summer (no earlier than $L_s=70°$ in the north or $L_s=250°$ in the south, although in most

220   cases color data exist from after the solstice), to rule out lingering seasonal frost. The

221   precise duration of seasonal frost depends on latitude, slope, aspect, and substrate (*cf.*

222   Vincendon et al., 2010; Dundas et al., 2019) but these bounds make seasonal frost

223   unlikely. Some sites were classified as confirmed but marginal. In these cases, the

224   morphology matched other scarps, but the coloration was weak or only occurred on a

225   small part of the scarp (Fig. 2a). Most scarps identified as candidates based on

226   morphology were confirmed to have at least some relatively blue coloration (in the cases

227   where HiRISE images exist), but some, particularly in Milankovič crater (Fig. 2b), have

228   coloration matching the surrounding terrain. The latter are likely to be exposures that are

229   partially or completely covered by an opaque coating of dust or debris, which is likely

230   thin since the morphology remains sharp. Alternatively, the ice at such scarps might

231   contain sufficient lithic material to suppress the coloration. Users of this data set may be

232   able to treat the probable scarps as confirmed if future HiRISE or other observations meet

233   the color criteria outlined above or yield spectral evidence of ice.

234   We considered the possibility that the scarps could be locations of year-round

235   frost stability rather than exposed subsurface ice. Frost on steep (~30°) mid-latitude

236   slopes such as crater walls near 45° latitude survives until $L_S\sim40°$ in the north and

237     $L_S\sim180°$ in the south; near 55°, it persists until $L_S\sim50°$ and $L_S\sim210°$, respectively

238   (Vincendon et al., 2010; Dundas et al., 2019). Near the poles H_2O frost survives into

239   summer on level ground (e.g., Appéré et al., 2011) and the very steep pole-facing scarps

240   have insolation roughly equivalent to the poles, although they receive more re-radiated

241   heat from other slopes. However, the scarps are erosional features, as they incise into and

242   remove surface material and have scarp-parallel ridges indicating past positions (Dundas

243   et al., 2018). Blocks falling from one scarp indicate an ongoing average retreat rate of

244   millimeters per Mars year (Dundas et al., 2018) and the same processes should act on

245   other scarps, which lack embedded rocks. Despite this, scarps retain relatively blue

246   coloration through the summer. Although some scarps possibly reach an equilibrium state

247   or even aggrade, the evidence that the scarps begin as erosional features, are actively

248   retreating at present, and yet retain the coloration of ice year-round is inconsistent with

249   persistent frost; the existence of morphologically identical scarps without icy coloration

250   also indicates that the scarp topography does not produce long-lived frost. Additionally,

251   CRISM band depth ratios at one scarp suggest coarse-grained ice rather than fine-grained

252   frost. Finally, scarp temperatures rise above the H_2O frost point (Dundas et al., 2018).

253   Thus, although there might be occasional cases of persistent frost, exposed ice is the

254   dominant explanation.

255   The quality and completeness of the THEMIS mosaics are generally good, and

256   the area where scarp pits might have been obscured or lost in data gaps is small. We also

257   spot-checked many patches with deep shading from topography by examining CTX

258   images and did not find any examples of pits or scarps hidden in this way. We used CTX

259   data to more closely examine pits and scarps found in THEMIS mosaics that appeared

260 consistent with the morphological criteria noted above. Those features are best seen when

261 kilometer-scale and larger, but smaller pits that appeared to match the morphology were

262 also inspected. Examination of hundreds of smaller or marginal-quality candidates gives

263 us confidence that the above criteria were effective in identifying scarps. Examining

264 every single pit or slope in the THEMIS-surveyed area at CTX resolution was not

265 practical. In regions of dense pitting such as scalloped terrain, we inspected those several-

266 hundred-meter scale features that appeared particularly sharp and distinct in the THEMIS

267 mosaics, and in the course of this survey we also examined large numbers of other pits

268 and slopes. This examination was sufficient to demonstrate that few scarps are not part of

269 the pits that are distinctive in the THEMIS IR mosaics, although some exist.

270 Additionally, survey results demonstrate that some scarps display gradations in

271 morphology. In aggregate, this survey likely includes nearly all sharply defined ice-

272 exposing scarps in the surveyed latitude zones that are near kilometer scale and larger.

273 This completeness scale is not well defined, but we estimate that it is between 500 meters

274 and 1 kilometer. Some smaller and less well-defined exposures are included here, but

275 more probably remain to be discovered. The two scarps reported by Harish et al. (2020)

276 were independently identified by our survey, supporting its effectiveness in identifying

277 scarps at these scales.

278 We measured scarp morphometric data in near-nadir HiRISE images.

279 Orthorectified images are not available for most sites, so precise geometric correction

280 was not possible and all dimensions are approximate, but for typical near-nadir viewing

281 geometry the distortion is small except on steep topography. Morphometric data include

282 the end-to-end straight-line distance, the greatest plan-view width, the estimated retreat

283   distance (between the scarp face and any geomorphic indication of the initiation point),

284   and the orientation of a line connecting the scarp endpoints.

285   Only one site has a high-resolution digital terrain model (DTM) (Dundas et al.,

286   2018). For some sites where appropriate images exist, we made slope estimates using the

287   shadow method of Dundas (2017b). This method takes advantage of the fact that for a

288   given Sun position and slope azimuth, there is a unique slope angle at which the slope

289   begins to cast shadows. We identified locations on the brink of self-shadowing by

290   selecting sections of slope with patchy coverage by local shadows. This method has two

291   major limitations. First, for any given Sun position it can only indicate particular

292   slope/aspect combinations, which may not be representative of the whole scarp and

293   certainly do not capture local variability. This could also result in biases when comparing

294   between sites, since the available images might favor different slope/aspect combinations

295   at different sites. Second, the method requires manual estimation of the downhill

296   direction. This is challenging, especially on curved slopes, and results in large

297   uncertainties. This method gives good results when applied to the scarp with a

298   corresponding high-resolution DTM, but the inherent limitations must be considered in

299   interpretation. Directional distortion due to map projection is minor for standard HiRISE

300   images, which are reprojected in equirectangular projection with a center latitude near the

301   image center.

302   We also documented the presence or absence of several possibly related

303   geomorphic features in the vicinity of the scarps. These include scalloped depressions (*cf.*

304   Morgenstern et al., 2007; Soare et al., 2008; Lefort et al., 2009; 2010; Zanetti et al.,

305   2010), expanded craters (*cf.* Dundas et al., 2015; Viola et al., 2015), and irregular pits, all

306   of which may indicate sublimation and ice loss, as well as surface lineations indicative of

307   flow (*cf.* Squyres, 1978; Milliken et al., 2003). These features were documented if they

308   appeared on the same material unit as the scarp and were within 10–20 km distance. For

309   confirmed scarps with HiRISE coverage, we also documented smaller-scale features of

310   the scarp-hosting unit within hundreds of meters of the scarp crest. These included

311   polygons (interpreted as created by thermal contraction cracking; Mellon, 1997), surface

312   boulders, which are of interest since their occurrence on top of deposits potentially

313   originating as snowpack is surprising, and indications of layering exposed by the scarp,

314   which could preserve a climate record.

315

316   *2.3. Ice-Exposing Craters*

317   New impact locations are usually identified by manual searches of images from

318   CTX or other medium-resolution images, where they appear as dark markings due to

319   disturbance of surface dust (Malin et al., 2006; Daubar et al., 2013). This leads to a bias

320   towards detecting new impacts in high-albedo, low-thermal inertia (dusty) regions. These

321   detections are also dependent on having before-and-after imaging to constrain their

322   formation dates, and the availability of such imagery varies spatially and temporally.

323   Follow-up with higher-resolution imaging from HiRISE is usually needed to confirm the

324   presence of a crater and determine its size. In some cases at middle and high latitudes, the

325   new impacts reach deeply enough to excavate ice. The ice gradually sublimates, causing

326   excavated material to change color to match the nearby regolith over a period of months

327   to years (Dundas and Byrne, 2010; Dundas et al., 2014). Hence, only impacts formed

328   within the last few months or years are reliable probes for ice. Unfortunately, sublimation

329   and the associated fading of the ice exposures are fastest at the lowest latitudes, where the

330   presence or absence of ice is least certain, implying that detection of ice is also least

331   efficient at those latitudes. At higher latitudes, the seasonal polar cap is particularly

332   effective at obscuring fresh impacts, as dark blast zones within the bounds of the seasonal

333   cap are erased within the first winter (Dundas et al., 2014) due to dust deposition or

334   redistribution, although ice sometimes remains distinct. Additionally, the dark markings

335   surrounding new impacts can fade within several Mars years, and more changes to the

336   blast zones are seen at higher absolute latitudes (Daubar et al., 2016), likely due to

337   seasonal processes, implying that the overall detections of new craters are less efficient at

338   high latitudes.

339   A strong theoretical and observational basis indicates that shallow ground ice is

340   almost ubiquitous poleward of ~45–50 °N/S and rare equatorward of ~30–35 °N/S (e.g.,

341   Mellon et al., 2004; Bandfield and Feldman, 2008; Pathare et al., 2018; Piqueux et al.,

342   2019), but the true boundary within that range is an unknown that can be tested with

343   observations of these craters. Therefore, we examined all new craters poleward of 35

344   °N/S and made an interpretation of the icy status based on the criteria discussed below.

345   We use HiRISE enhanced color observations as our primary means of determining

346   whether ice is likely exposed. The ice exposed by craters is bright and generally appears

347   relatively blue or relatively white in HiRISE enhanced color. Relatively white coloration

348   is uncommon in non-polar HiRISE images and with appropriate context can be highly

349   indicative of frost or ice. Relatively blue coloration can also be due to mafic materials

350   (Fig. 3a), but we treat it as indicative of ice when other evidence is strongly supportive of

351   this interpretation: i.e., the material is substantially brighter than surroundings rather than

352 simply distinct in color. An additional indicator of ice is that material is distinct from

353 other ejecta and crater floor materials, suggesting that some ejecta is ice and some is ice-

354 free even if both are relatively blue. This is expected because the Martian surface is

355 mostly mafic, even when ice is present. For small exposures, the ice is often in discrete

356 patches with a distinct color relative to other excavated material. Other than the initial

357 decision to only examine craters above 35°, latitude was not used to interpret the

358 presence of ice, since the distribution of ice is not completely understood. Some material

359 interpreted as ice was slightly relatively yellow, but substantially brighter than the

360 surroundings and in settings where thermal contraction polygons also strongly support

361 the presence of subsurface ice. Possible ice with a relatively yellow coloration has been

362 reported in a gully alcove elsewhere on Mars (Khuller and Christensen, 2019), so this

363 coloration is consistent with the presence of ice as well.

364 　　　　CRISM can provide definitive spectral tests for ice in some cases where the

365 exposure is large enough (Byrne et al., 2009), but we do not use this as part of our

366 diagnostic process because most of the marginal cases are small (2–10 m diameter

367 craters) and unlikely to produce an unambiguous spectral signal in 18 m/pix CRISM data.

368 In many cases appropriate CRISM observations do not exist. Three factors, however,

369 support a general interpretation of the impact features meeting these color criteria as icy,

370 rather than exposed salts or other bright lithic material: (1) CRISM confirmation of ice at

371 several sites that share the indicators that we use for ice (Byrne et al., 2009); (2) lack of

372 spectral detections of other materials that might account for the bright deposits; and (3)

373 fading and disappearance over time consistent with sublimation at many of these sites

374 (Dundas and Byrne, 2010; Dundas et al., 2014). Since there is a strong theoretical basis to

375   expect ice at these latitudes and cryogenic landforms are common around the craters, this

376   is the simplest interpretation; as discussed below, our diagnostic criteria are likely

377   underestimating the occurrence of ice.

378   We also note candidates where we consider the evidence for ice to be less

379   compelling. These are divided into (1) probable ice, where ice is our preferred

380   interpretation but not considered definitive due to very small size, weaker color contrast

381   with other ejecta, or lack of a well-defined crater; and (2) possible ice, where there is a

382   small color feature in the crater with minor contrast, or a bright feature that could be due

383   to topographic effects. Some sites initially classified as possible or probable were later

384   elevated to confirmed if the candidate exposure became less distinctive over time in a

385   manner consistent with sublimation and lag development (i.e., a color feature reverting to

386   match adjacent surfaces more quickly than the general fading of the blast zone).

387   Some low- and mid-latitude impacts (e.g., Fig. 3b) expose relatively bright

388   material that contrasts with a dark surface but is not interpreted as icy. Few of these exist

389   in our study latitudes. The surface geomorphology surrounding these sites generally does

390   not suggest ice (in particular, no polygons are interpreted as thermal contraction cracks).

391   Most of these craters occur at low latitudes (<35°) outside our survey area, where

392   theoretical models suggest that shallow ice is unlikely (e.g., Mellon et al., 2004).

393   Additionally, most or all of the ejected material is bright rather than isolated patches. At

394   low latitudes ice should be covered by a significant thickness (>1 m) of regolith or it

395   would otherwise sublimate rapidly, so if there were ice, it would occur in the ejecta as a

396   mix of ice and non-icy regolith. These bright ejecta deposits may be similar to exposures

397   of bright material by rover wheels in Gusev crater (e.g., Rice et al., 2011) or other

398 surface/subsurface compositional or grain size differences. While these craters provide

399 information about the Martian subsurface, they are not considered further in this

400 discussion of subsurface ice.

401   The icy craters that we document are those that expose persistent bright ice that

402 remains distinct for months to years while sublimating, indicating clean ice with a low

403 lithic content. Some apparently non-icy craters may have exposed subsurface pore ice,

404 which would be all but impossible to detect from orbit. As shown by the Phoenix lander

405 excavations, exposed pore-filling ice is dark, and in summer at mid-to-high latitudes it

406 sublimates enough to create a surface coating that is indistinguishable from regolith

407 within days (Mellon et al., 2009; Smith et al., 2009). This is much shorter than the typical

408 time between the impact and acquisition of HiRISE images. Candidate impacts at high

409 latitude are usually imaged by HiRISE within weeks of the initial detection in lower-

410 resolution images, but that initial detection can be one to several years after the crater

411 formed. One caveat is that the impact process may generate fractures and fine-grained

412 material, which would be brighter than the pore ice exposed by the Phoenix lander, but a

413 small amount of sublimation would still quickly produce an opaque cover under those

414 conditions. Additionally, the small size of many of these craters means their shallow

415 depths of only tens of centimeters may not be enough to reach the ice table. Finally, at

416 high latitudes the seasonal cap reworks the surface, removing blast zones and obscuring

417 ice, which can preclude detection and confirmation if craters are not imaged or re-imaged

418 before winter. Thus, the set of craters we consider confirmed ice exposures are a

419 minimum, and subsurface ice could exist at other known or unknown impact locations.

420

3. Scarp Observations

The full set of scarp exposures is given in Tables S1–S2 and mapped in Fig. 4. Below, we discuss some relevant morphological and geographical observations.

3.1 Scarp Distribution

In the southern hemisphere, 21 confirmed exposure sites were identified in the southern hemisphere (some with multiple scarps), along with two candidates lacking ice coloration, and one for which no HiRISE color data were available at the time of writing. The southern-hemisphere scarps are confined to a narrow range of longitudes near the Hellas basin, not evenly distributed throughout the latitude band. Most of the exposures are between 80–115 °E longitude and 50–61 °S latitude, similar to those previously known. A few occur in scalloped terrain (*cf.* Zanetti et al., 2010) at 50–61°E and a small cluster near 137 °E.

Scarps in the northern hemisphere are strongly concentrated in the mantling deposits within Milankovič crater (54.5 °N, 213.5 °E), which we subdivided into four sites in Table S1 based on the four cardinal directions. Over 70 features have the morphology of ice-exposing scarps at this location, although in HiRISE data some lack the relatively blue coloration indicative of exposed ice. Beyond Milankovič, a handful of scarp sites occur in crater-fill materials farther east, and one occurs in northern Utopia Planitia (96°E).

3.2 Scarp Morphology and Morphometry

443   Most scarps have a simple morphology (e.g., Fig. 1b), but a few have several

444   subparallel faces (Fig. 5) or are divided into adjacent segments. Many exhibit faint, crude

445   layering or color banding, but distinctive sub-meter-scale layers are uncommon (Fig. 6).

446   Scarp lengths range from 200 m–6.5 km, and plan-view scarp widths range from 20–200

447   m. Length, width, and estimated retreat distance are loosely correlated (Fig. 7a, b).

448   Latitude appears to weakly influence the upper envelope of scarp retreat distance, with

449   somewhat greater scarp retreat at lower latitude (Fig. 7c). This may indicate active

450   formation of new scarps, coupled with faster retreat at lower latitudes, because retreat

451   distance should be a function of scarp age and sublimation rate. The latter will be

452   influenced by latitude. However, the ratio of scarp length to retreat distance (the plan-

453   view aspect ratio of the pits) shows no trend with latitude (Fig. 7d). This aspect ratio

454   indicates the extent to which the scarp widens as it retreats. All scarps in both

455   hemispheres approximately face the pole but most are oriented slightly east of due

456   poleward, with a typical offset from N/S of 5–10°. This offset could relate to

457   morning/afternoon asymmetries in temperature combined with the thermal inertia of the

458   surface reducing peak temperature. Individual scarps have along-scarp orientation

459   variations on the same order as this offset.

460   The one scarp for which high-resolution topographic data exist (southern scarp

461   #1) has typical slopes of ~45° with moderate variations both vertically and laterally

462   (Dundas et al., 2018). Shadow-derived estimates at four locations on this scarp are 47–

463   49°, demonstrating that the method gives reasonable results for typical scarp geometry.

464   Shadow-derived slope estimates for other scarps with appropriate shadow conditions are

465   given in Table S3. In the southern hemisphere, slopes range from 41–60°, with most

466 between 45–50°. In the north, a variety of confirmed and candidate exposures have slopes

467 of 40–64°. The mean slope in the north (53°) is similar to that in the south (49°). These

468 estimates suggest that southern scarp #1 is typical. These slopes indicate that the plan-

469 view widths of the scarps approximate the vertical relief to within a factor of 2.

470 Furthermore, the pits do not necessarily reach all the way to the bottom of the ice, so the

471 ice thicknesses may be even larger.

472 As reported in Dundas et al. (2018), scarp-parallel features indicate that scarps

473 retreat generally equatorward and that retreat is uniform along the length of the scarp.

474 Triangular or other shapes of the resulting pits indicate that the scarp width can vary over

475 time (Fig. 8). Scarp retreat appears to be close to uniform along the length of the scarp,

476 such that when the retreat direction is oblique rather than normal to the scarp, the

477 orientation of the scarp remains unchanged (Fig. 8). Notches in the plan-view shape of

478 pits (Fig. 8) suggest that scarp retreat occasionally reactivates only over part of its length;

479 the other parts may reactivate later, giving rise to the small parallel outliers seen in some

480 pits. The aspect ratio of the scarp pits shows substantial scatter (Fig. 7d), so the rate at

481 which scarps widen as they retreat is highly variable.

482

483 *3.3 Scarp Setting*

484 The regional properties of the locations are broadly similar in both hemispheres.

485 All of the identified scarps occur within deposits that appear to mantle the regional

486 surface (Fig. 9); although in a few cases, the uppermost part of the mantling deposit may

487 have been removed (Fig. 9c). In the southern hemisphere, the kilometer-scale regional

488 slopes around the scarps and pits are mostly pole-facing but generally low (typically ~5°

489   in the Mars Orbiter Laser Altimeter digital elevation model), and some are nearly flat.

490   The scarps there are often associated with the slopes of few kilometer-scale local massifs

491   or crater walls. In the northern hemisphere, the vast majority of scarps and candidate

492   scarps are in Milankovič crater. They are found on all slope orientations therein, but

493   primarily on the west side of the crater (Fig. 10). As in the south, the regional slopes are

494   generally low. The material on the slopes of the crater may have a low density (at least

495   within the upper 5 meters) as it has a low radar surface reflectivity (Morgan et al., 2020).

496   The other northern-hemisphere candidates are found within materials that infill few

497   kilometer-scale impact craters. The regional albedos from the Thermal Emission

498   Spectrometer (TES; Christensen et al., 2001) are all close to 0.2, and the regional

499   apparent thermal inertias from TES (Putzig and Mellon, 2007) are between 128–225 J m^{-2}

500   K^{-1} s$^{-0.5}$, consistent with a surface layer of unconsolidated dry soil a centimeter or more

501   deep, with the sole exception of the site in Utopia.

502   Although the scarps are characteristically within mantling deposits, the associated

503   geomorphology is variable. Candidate ice-loss features (scalloped depressions and

504   expanded craters) are found near some of the scarps, but in most cases the landforms are

505   not well-defined examples. However, irregular pits that do not closely match the

506   scalloped or expanded morphologies are almost ubiquitous across the scarp-hosting

507   mantling deposits. Arcuate lineations indicative of ice flow are uncommon. In the plateau

508   material at the top of the scarp, polygons (likely due to thermal contraction of ice) are

509   common but not ubiquitous, and often not well defined, which may indicate that the ice is

510   deep enough to not experience strong thermal cycles or that it anneals effectively without

511   infall of material into the cracks. In some cases the surface material consists of aeolian

512 bedforms and so may currently be too mobile to develop defined polygons. The brink of

513 the scarp is often broken into blocky fragments that might be defined by subtle polygonal

514 fractures that have generated little surface relief. Polygons are also common on the walls

515 and floors of some pits. The upper surface of the scarp-forming material usually has few

516 boulders, particularly in the northern hemisphere.

517   CRISM data confirm exposed ice at several scarps (Table S1) beyond those

518 described in Dundas et al. (2018). Detections at two of the scarps were independently

519 confirmed by Harish et al. (2020). Notably, one observation of the icy scarp at 57 °N,

520 95.7 °E (northern scarp site #4) shows a distinct water ice signature, as well as an

521 ambiguous spectral signature in the visible to near-infrared, suggesting impure ice. The

522 simultaneously acquired HiRISE image shows only a weak color signature covering parts

523 of the scarp, leading to a classification of confirmed but marginal. This suggests that all

524 scarps with the classic morphology could be ice exposures, regardless of coloration.

525 Either the covering lag is too thin to completely suppress the ice spectral signature or the

526 lithic content of the ice is high enough in some cases that the coloration seen in HiRISE

527 is minimal. If the coloration is from a lag coating, it must be very thin, as a dust coating

528 of tens of microns can be opaque at visible wavelengths (Wells et al., 1984; Fischer and

529 Pieters, 1993). If the coloration reflects the bulk ice composition, this is still consistent

530 with a high ice content. Cull et al. (2010) show that for as little as 10 weight % lithics

531 (>95 volume % ice) the visible color contrast may be minimal, and Clark and Lucey

532 (1984) showed substantial darkening and weak spectral absorption features for even

533 smaller amounts of non-ice material, depending on its albedo. Further monitoring with

534 HiRISE might distinguish between these possibilities, as lags could be removed

535 episodically. Harish et al. (2020) also noted some scarps at northern scarp site #5 with

536 relatively blue coloration but no spectral signature of ice, likely because the scarps were

537 substantially shadowed.

538   Numerous pits were examined and determined not to meet the morphological

539 criteria for likely ice exposures. Some of these may be former scarps that have become

540 buried under sublimation lags that are thick enough to obscure the sharp morphology of

541 clean exposures. Examples of pits without distinct scarps are shown in Fig. 11 for

542 comparison, and Fig. 8 shows a pit that mostly lacks exposures apart from a small outlier

543 scarp.

544

545 **4. Crater Observations**

546   HiRISE images now cover 48 ice-exposing impact sites (Fig. 12 and Table S4).

547 The diameter of ice-exposing and non-ice-exposing craters poleward of 35 °N/S is shown

548 in Fig. 13. Diameter scales linearly with maximum excavation depth for small craters

549 (Melosh, 1989), and Fig. 13 also shows 0.084× the crater diameter. This value is given

550 since the maximum excavation depth is ~1/10 of the transient crater diameter and the

551 transient crater is ~0.84× the final diameter for simple craters (Melosh, 1989); although

552 seemingly precise, this depth should only be treated as an approximation. The data set is

553 more extensive than that in Dundas et al. (2014) but is broadly similar and does not

554 change the interpretations made therein. Those include the widespread occurrence of

555 clean ice with local heterogeneity, as well as the latitudinal distribution in the northern

556 hemisphere, which suggests that the long-term atmospheric water vapor content was

557 higher than at present and/or that there is a near-surface concentration of vapor. The

558   morphology of the ice exposures ranges from small fractions of the crater interior to

559   extensive icy ejecta. Several important new observations and their interpretations are

560   discussed below.

561   Weak material over a strong layer produces characteristic crater morphologies of

562   flat floors and benches or terraces for craters with diameters approximately 4–10 times

563   the weak layer thickness (Quaide and Oberbeck, 1968). The depth to the strong layer can

564   be estimated using the methods of Bart (2014). For sites with exposed ice, there is a high

565   likelihood that such a strong layer is the top of the ice table since the ice is known to exist

566   and should provide a strength contrast. We apply this method at sites with multiple flat-

567   floored craters. Those craters are often not the same as those with visible ice, since the ice

568   exposures tend to be in the largest craters that penetrate more deeply into the ice table.

569   (For sites without confirmed bright ice, the morphology could be produced by pore ice

570   but also by shallow bedrock or another strength contrast, making the interpretation less

571   certain.) The results (Table 1) show significant variability in depth to the strong layer

572   between different craters in individual clusters. This likely reflects both real local depth

573   variation and measurement uncertainty. In combination with differences in the visibility

574   of ice in similarly sized craters (Dundas et al., 2014), this indicates that heterogeneities in

575   the ice table depth and ice content are significant at scales of tens to hundreds of meters.

576   Fewer new craters (icy or not) have been discovered in the southern hemisphere

577   in comparison with the north, mainly because the less extensive dust cover in the south

578   inhibits detection, but also due to different imaging and search techniques that vary by

579   region. The distribution is still sufficiently sparse that the southern latitudinal boundary is

580   not well defined. However, the number and distribution of icy impacts observed in the

581   southern hemisphere has expanded significantly relative to Dundas et al. (2014), and the

582   lowest-latitude ice detection in the south is now at 46.2 °S. That crater is on a slight pole-

583   facing slope with nearby gullies and thus may not be representative of level ground, but

584   there is also a probable candidate on flat ground at 42.6 °S.

585   In the northern hemisphere, the lowest-latitude detection remains at 39.1 °N. This

586   location is part of a southward excursion of icy crater detections extending between

587   ~145–205 °E where ice detections are common between 40–50 °N (Fig. 12). This

588   contrasts with a lack of confirmed icy craters at those latitudes between 205–255 °E. The

589   region lacking icy craters corresponds to terrain where stability models predict that ice

590   should be quite shallow and extend particularly far towards the equator due to high

591   albedo and low thermal inertia (Mellon et al., 2004), so it is possible that pore ice is

592   dominant at the top of the ice table there. Some of the non-ice-exposing craters in this

593   area have flat floors which could indicate such a pore ice table, but this interpretation is

594   nonunique. At other longitudes, new crater detections between 40–50°N are sparse, and

595   the only other ice detections equatorward of 47.4 °N are on lineated valley fill; these

596   detections may not indicate extant ice under the surface in those areas apart from within

597   the lineated valley fill.

598   Two craters near Protonilus Mensae excavated lineated valley fill and confirm the

599   presence of ice within a few meters of the surface there between 41–42 °N (Fig. 14). This

600   could be the top of glacial ice that has been detected in similar material by the Shallow

601   Radar (SHARAD; Holt et al., 2008; Plaut et al., 2009; Petersen et al., 2018), the top of

602   which is not detectable at SHARAD resolution (approximately 10 m in ice); however,

603   ice-rich lenses or other structures within a thicker debris cover cannot be ruled out. In the

604   eastern part of the crater shown in Fig. 14a, ice exposed in the crater wall appears to

605   make up the core of a surficial topographic ridge (a part of the surface type sometimes

606   referred to as "brain-coral" or "brain" terrain (e.g., Noe Dobrea et al., 2007; Levy et al.,

607   2009b)) that was cut by the impact, providing information about the subsurface structure

608   of such material. In both of these craters the visible ice exists mostly in discrete blocks, in

609   contrast with most others; this suggests that the shallow subsurface ice is in discrete

610   bodies surrounded or covered by ice-free debris, which may indicate that ice at these

611   locations is unstable and sublimating, since ice would be expected to cement the regolith

612   pore space at these depths if it were stable.

613   Polygons attributed to thermal contraction cracking (e.g., Mellon, 1997) are

614   nearly ubiquitous at the sites of ice-exposing impacts. They are occasionally found

615   around new impacts where HiRISE images do not show bright ice but much less

616   frequently. At some of those sites impacts probably exposed pore ice or did not excavate

617   to the depth of the ice table. This suggests that thermal-contraction polygons and present-

618   day ice are strongly correlated and that relict ice-free polygons are uncommon. However,

619   the morphology of the polygons is diverse, including high-centered and low-relief

620   features, irregular or incomplete polygon networks, as well as regularly spaced low-relief

621   hummocks without defined fractures. Thus, the relationship between the detailed polygon

622   morphology observable at HiRISE resolution and the presence of excess ice is not simple,

623   but ice-exposing craters are sparse and offer limited information about the vertical

624   structure of the ice.

625   An 18 m-diameter crater that formed on the south polar layered deposits (SPLD)

626   during southern winter of Mars Year 34 showed minimal bright ice once the seasonal

627 frost had vanished (Fig. 15ab) and was classified as probable. This crater is discussed

628 more extensively in Landis et al. (2020). A second crater cluster in the southern mid-

629 latitudes has been observed to form with ejecta superposing seasonal frost (Fig. 15c).

630 This site also lacks bright ice once defrosted, but the craters are much smaller and may

631 not have excavated to ice. In both cases the crater morphologies appear minimally

632 affected by the presence of CO_2 frost at the time of impact, demonstrating that seasonal

633 frost probably has little effect on the long-term cratering record except for extremely

634 small craters.

635   The SPLD and Protonilus craters also enable us to assess whether any of the

636 observed bright ice is due to melting/refreezing (*cf.* Reufer et al., 2010) or condensation

637 of vapor post-impact, rather than representing the original state of ground ice. If the

638 former were the case those effects would be expected to be strongest in the largest

639 craters, which represent the most energetic impacts. Small bolides should be slowed by

640 the atmosphere and their small craters should have little if any melting, so we can rule out

641 the possibility of impact generation of clean ice if it does not occur in the larger craters.

642 The 18 m crater on the SPLD (Fig. 15a, 15b) is larger than most lower-latitude craters

643 with visible ice exposures but has negligible amounts of bright ice. The SPLD certainly

644 contains significant ice content in bulk (at least 85%; Plaut et al., 2007; Zuber et al.,

645 2007) although the near surface could be pore-filling ice, and theory indicates that ice

646 should begin at depths of centimeters there (e.g., Mellon et al., 2004). Likewise, discrete

647 ice blocks occur around the largest ice-exposing crater (Fig. 14a) as well as several

648 others. Long-baseline temporal monitoring of several craters demonstrates shrinking and

649 disappearance of blocks of ejected ice, as reported at other sites by Dundas et al. (2014),

650   suggesting that the blocks are massive ice. These blocks are inconsistent with melt pools

651   or condensation. Thus, several of the largest ice-exposing craters have characteristics that

652   show that the bright ice is not produced by the impact process. This implies that the

653   observed clean ice represents the natural state of the pre-impact ice for most or all craters.

654   High ice contents (well above pore-filling) are widespread in the shallow subsurface at

655   latitudes above ~40 °N.

656   Only five of the confirmed ice-exposing impacts have an H_2O ice signature in

657   CRISM data (Table S4), while 23 have CRISM data without an ice detection. All five are

658   among the larger craters or clusters of several craters and have large swaths of ice in their

659   ejecta rather than small exposures in the crater itself. In some locations, we also analyzed

660   repeat CRISM observations, but the absorption bands attributed to water ice were weak

661   and barely detectable above the noise. Either atmospheric haze, accumulated surface dust,

662   or spectral mixing and signal being averaged into multiple pixels precluded detection of

663   ice in the later CRISM images after the initial observation. This demonstrates that

664   extensive areal exposures and contemporaneous observations are required for ice

665   detection by CRISM, as even the largest ice exposures only occupy portions of a handful

666   of pixels.

667

668   **5. Discussion**

669   *5.1. Importance of Subsurface Ice Exposures*

670   These surveys of scarps and craters directly provide information about the nature

671   and distribution of subsurface ice on Mars. They also provide an extensive set of

672   locations that can be used for validation of the presence and properties of ice indicated by

673   other data and models. While they have not been studied in situ, these locations provide

674   more direct and localized information on the state of the ice than other methods currently

675   available. This level of verification and detail is useful for interpreting other data sets

676   (e.g., Pathare et al., 2018; Piqueux, et al., 2019), for design of possible ice-detection

677   instruments (e.g., Haltigin et al., 2018), and for the possible use of ice by human

678   explorers (*cf.* Heldmann et al., 2014; Putzig et al., 2020).

679   Both the craters and scarps provide information about the local state of the ice

680   table, but the difference in the nature of the exposure and exposure process poses

681   challenges for analyzing the two together. For instance, impact-exposed ice is often

682   relatively white while the scarps are generally relatively blue. This may indicate some

683   degree of impact modification (e.g., fracturing reducing the grain size or increasing

684   porosity). Additionally, these differences in relative color could in part be related to the

685   surrounding terrain. Quantitative photometry including assessment of topography and

686   atmospheric scattering is needed before such color differences can be confidently

687   interpreted. The craters represent semi-random samples (subject to detection biases),

688   while certain regions or certain ice properties may be conducive to scarp formation, as

689   discussed below. Finally, different properties are measurable for each: for instance,

690   craters primarily provide information on the depth to ice. Scarps place lower bounds on

691   the ice thickness, but the depth to the top of the ice may be obscured by material falling

692   from the scarp crest. Despite this, in some places ice, can be seen within 1 m of the scarp

693   crest (Dundas et al., 2018) and could be exposed by craters.

694   The expanded surveys presented here are generally consistent with previous

695   interpretations of the state and distribution of ice based on a more limited sampling of

696   features (Dundas et al., 2014; 2018). The larger data sets presented here do provide

697   several new insights into the origins, properties, and distribution of subsurface ice,

698   discussed in the following sections.

699

700   *5.2. Distribution, Properties, and Origins of Subsurface Ice*

701   The lowest-latitude detection of ice based on craters is unchanged in the north

702   compared with Dundas et al. (2014). Exposure of clean ice by new impacts is common,

703   indicating that such ice is widespread at shallow depths. The poleward-shallowing trend

704   of ice in crater exposures reported by Dundas et al. (2014) is confirmed by the additional

705   data reported here, with depth and latitudinal boundary similar to theoretical predictions.

706   Poleward of ~50 °N/S latitude, most dated new impacts either definitely or possibly

707   expose bright ice. In crater clusters the larger craters generally expose bright ice and the

708   smaller ones do not (Table S4), but in several instances this relation is reversed. The

709   latter requires lateral heterogeneities in the distribution or concentration of ice in the

710   upper meter of the subsurface or variable impact properties and distribution of ejecta. The

711   depth to ice also has significant local variability when measured within crater clusters

712   (Table 1), consistent with theoretical predictions (Sizemore and Mellon, 2006) and

713   excavations by the Phoenix lander (Mellon et al., 2009).

714   The apparent variation in icy crater detections between 40–50 °N, from frequent

715   icy craters between 145–205 °E to a lack at 205–255 °E, corresponds with features in

716   several other data sets. This zone of low-latitude icy craters corresponds to a region

717   where neutron spectroscopy shows high ice content (greater than pore-filling) extending

718   to lower latitudes than in the rest of the northern hemisphere (Pathare et al., 2018). The

719   transition near 205 °E approximately matches the transition from abundant expanded

720   craters (to the west) to few (to the east) in the mapping of Viola et al. (2015), although

721   that map has little coverage west of 190 °E. Viola and McEwen (2018) show that

722   expanded craters equatorward of 40 °N are concentrated between 185–205 °E. The zone

723   of icy craters also corresponds to radar detections of a low dielectric constant (interpreted

724   as indicating a high ice content extending to tens of meters depth), which are

725   concentrated between 180–215 °E (Bramson et al., 2015) and interpreted as a regional ice

726   sheet. The high bulk ice content of this unit has been challenged based on radar loss

727   tangent estimates (Campbell and Morgan, 2018), but the agreement of the ice exposures

728   and neutron spectroscopy suggests that at least the upper centimeters of the material are

729   ice-rich, which is further supported by the observation of expanded craters (Dundas et al.,

730   2015).

731   A similar ice sheet has been proposed in the Utopia region (Stuurman et al., 2016)

732   based on mapping of radar reflectors that indicated a dielectric constant similar to that of

733   ice. No new impact detections are in the region of radar reflectors mapped by Stuurman

734   et al. (2016), likely because a lack of surface dust makes such detections rare (Fig. 12).

735   However, one ice-exposing crater is within the broader geomorphic unit of mesas and

736   scalloped depressions (Kerrigan, 2013) that contains the reflectors. Such scalloped

737   depressions have been attributed to partial sublimation of an ice-rich unit (e.g.,

738   Morgenstern et al., 2007; Lefort et al., 2009; Zanetti et al., 2010; Dundas et al., 2015), the

739   top of which may be indicated by the crater exposure.

740   Scarp exposures provide relatively weak constraints on the global distribution and

741   properties of ice on Mars, since they are at higher latitudes than many of the craters and

742   may not reflect the typical state of shallow subsurface ice. However, they provide

743   important constraints on local properties. The scarps generally occur in surface-mantling

744   deposits. Mantling deposits that have been interpreted as ice-rich are common at middle

745   to high latitudes (e.g., Mustard et al., 2001; Head et al., 2003; Milliken et al., 2003;

746   Schon et al., 2009); the scarp regions appear somewhat more extensively mantled than

747   other areas, but this is difficult to quantify. The fact that scarps occur only in a narrow

748   latitude band in both hemispheres suggests that some process controlled by latitude is

749   important to exposing the ice, meaning that similar ice could exist elsewhere. However,

750   since the scarps are concentrated at certain longitudes while ground ice is expected to be

751   ubiquitous at these latitudes (e.g., Mellon et al., 2004; Schorghofer and Aharonson, 2005;

752   Chamberlain and Boynton, 2007), some other factor(s) relating to the state of ice or the

753   physical processes exposing it is also necessary to explain the scarp distribution. These

754   observations can be explained if ice exposures occur within a subset of mantling deposits

755   where ice is particularly thick and/or pure, providing longitudinal or local control, and if

756   particular latitudinal conditions (e.g., insolation and temperature) are required to create

757   and maintain the exposure. Supporting this possibility, the scarps in the southern

758   hemisphere are mostly located in longitudes where neutron spectrometer data show high

759   ice contents (60–90 weight percent) extending to relatively low latitudes (Pathare et al.,

760   2018). The same region also overlaps the location of the largest concentration of

761   scalloped depressions and thermokarst landforms in the southern hemisphere (Zanetti et

762   al., 2010; Viola and McEwen, 2018), also consistent with high ice contents. Scarps and

763   their host mantling units often appear localized near massifs or crater walls, which might

764   help concentrate snow deposition in incipient glaciers, but these correlations with other

765 data sets suggest that the scarp-hosting ice bodies are associated with high regional ice

766 contents. In this interpretation, the ice at the exposures represents an ice-rich end-member

767 of the diversity of Martian near-surface mantling and ice deposits. Fully testing this

768 hypothesis requires more information on the state of ground ice at locations without

769 scarps; crater exposures are too shallow to provide a full comparison.

770   The ice exposed in the scarps likely originated as snow or frost, which has now

771 been compacted. This is based on two main lines of evidence. First, the hosting units

772 typically drape the surface in a manner consistent with atmospheric deposition rather than

773 infilling topographic lows, and the scarp properties imply a very low lithic content

774 (Dundas et al., 2018). Second, the fine crosscutting layers observed at some scarps (Fig.

775 6) are most consistent with snow, since subsurface growth of ice lenses or other

776 structures (e.g., Sizemore et al., 2015) would likely parallel the surface and not produce

777 crosscutting relationships. (This could arise within an airfall deposit that was partially

778 eroded and then covered, but the high ice content (Dundas et al., 2018) is better explained

779 by snow or frost.) Moreover, non-snow theories for the development of high subsurface

780 ice contents on Mars, such as ice lens growth or enhanced vapor diffusion (e.g., Fisher,

781 2005; Sizemore et al., 2015) operate in the near surface rather than building units >100 m

782 thick.

783   The presence of boulders on the surface of scarp-hosting units was noted as a

784 puzzle by Dundas et al. (2018). If the massive ice deposits are consolidated snow, they

785 should lack clasts larger than windblown sand or dust. The additional scarps included in

786 this larger sample set mostly exhibit few or no surface boulders at the top of the unit. This

787 observation is more favorable for a snowpack model than are abundant boulders, but the

788   presence of any large rocks remains a puzzle. Rocks can be concentrated by sublimation

789   processes (Aylward et al., 2019), but must be present initially. Indications of glacial-style

790   flow are rare at these locations, so rafting to concentrate rocks at the surface may be an

791   insufficient explanation for boulders superposing the ice. An alternative is that boulders

792   are lifted and held at the surface during ice accumulation (Schorghofer and Forget, 2012),

793   but boulders are embedded within ice at one scarp (Dundas et al., 2018). A similar

794   process of locking boulders within seasonal CO_2 frost and moving them via differential

795   thermal contraction is a possible explanation for horizontal boulder sorting at other

796   locations (Orloff et al., 2013). An additional possibility is that these surface boulders are

797   ejecta from nearby impact craters, although the sparse craters on the surface of the

798   mantling deposits suggest that impacts since those deposits were emplaced were not

799   sufficient. The scarps surveyed here are distinctly different from the steep slopes at the

800   edge of the north polar layered deposits (NPLD), which have slopes up to 70° over 300-

801   meter baselines and are approximately vertical over some shorter intervals (Russell et al.,

802   2008). These slopes also occur in a body of ice with low dust content, estimated to be

803   <2% (Picardi et al., 2005). Despite active avalanching and slope retreat (Russell et al.,

804   2008), the NPLD scarps generally have dusty coloration except on the flat residual cap

805   (Byrne, 2009), although because this is inferred from relative color, quantitative

806   inferences about the ice content are difficult.

807   In comparison with the scarps, the craters provide relatively little constraint on the

808   deposition and modification processes of the ice. They demonstrate the widespread

809   occurrence of processes that create high ice contents in the shallow subsurface, but the

810   small penetration depth and exposure size, and disruption of the ice by impact, make it

811   difficult to distinguish between the various candidate processes. Boulders are common

812   around many of the craters, as at the scarps.

813

814   *5.3. Scarp Formation and Evolution*

815   The scarps pose a significant puzzle: how is the bare ice exposure created and

816   maintained, when a covering lag is expected to develop within years and sublimation is

817   actively occurring? Landscape evolution modeling suggests that a steep exposure of

818   dusty ice would gradually become shallower because the base would be buried under the

819   debris released by its own sublimation and retreat (Dundas et al., 2015). The straight

820   geometry of the scarps may reduce this effect because the debris at the base is not

821   collected from a wide area. The scarps are quite steep and could shed debris rather than

822   accumulating a surface cover, like the steep slopes of parts of the NPLD (Russell et al.,

823   2008). This appears to be occurring in some cases, but in at least one example the process

824   is building a debris-covered lower slope and deactivating sublimation on the lower scarp

825   (Dundas et al., 2018). Some scarps may be partially or completely debris covered (Figs.

826   2b, 8, 11), so in some conditions this process may cease. Additionally, how such a slope

827   is created in the first place or how scarps reactivate after accumulating surface debris is

828   not obvious. The scarps do not resemble impact features, which are typically circular, but

829   runaway growth from small impacts is a possibility. Fault movement can be ruled out at

830   one location by a lack of vertical offset (Dundas et al., 2018), and at no site is there any

831   indication of fault-like deformation extending beyond the scarp. Additionally, ridges

832   indicating scarp retreat are inconsistent with movement on a fault. The scarps face the

833 pole regardless of the slope orientation and sometimes occur on level surfaces, which

834 rules out any gravity-driven failure.

835   Two possible factors in creating and maintaining scarps are seasonal frost and

836 aeolian transport. CO_2 frost can transport material either via basal sublimation (e.g.,

837 Kieffer, 2007; Pilorget and Forget, 2016) or by loading a steep slope and avalanching as

838 observed at the NPLD (Russell et al., 2008), and winds could also strip away a

839 sublimation lag. The gradual fading of color contrast and weakening of ice spectral

840 signatures on one scarp over the course of a summer (Dundas et al., 2018) were

841 consistent with frost effects, as a lag might accumulate over the summer before being

842 removed by frost in the following winter and spring, and lineations suggesting frost-

843 driven mass wasting occur on scarps in early spring images (Fig. 16a). The latitudinal

844 dependence of scarp occurrence is consistent with a role for CO_2 frost but would require

845 some additional control, since such frost is ubiquitous in the winter at middle and high

846 latitudes, and the abundance on the scarps is not known. Frost and wind effects are not

847 mutually exclusive. Ridge structures at some scarp locations (Fig. 16b) resemble features

848 interpreted as dust bedforms (Geissler, 2014) or indurated dust (Bridges et al., 2010)

849 elsewhere on Mars. These are oblique to the scarp and cut by it, suggesting limited

850 mobility relative to the scarp retreat timescale. For comparison, modeling of sublimation

851 conditions at migrating NPLD trough sites suggests that removal of a sublimation lag by

852 surface winds is likely necessary for sublimation to continue over prolonged periods there

853 (Bramson et al., 2019).

854   Cliffs on terrestrial debris-covered glaciers offer both insights and contrasts. Cliff

855 exposures can be created by sliding of the debris layer, or collapse into lakes or meltwater

856   conduits (e.g., Kirkbride, 1993; Sakai et al., 2002). Neither of these is likely on Mars,

857   given the low slopes and lack of a significant meltwater system at Martian temperatures.

858   In the Himalayas on Earth, equator-facing slopes are quickly covered by debris, while

859   pole-facing ice cliffs persist and act as important drivers of ice loss, because they receive

860   less insolation and are steep enough to shed debris (Sakai et al., 2002; Buri and

861   Pellicciotti, 2018). Differences in the radiative balance of the upper and lower parts of the

862   slope as a function of aspect are important to the development of the cliffs: at some

863   aspects, melting and retreat of the lower slope is enhanced, helping to maintain a steep

864   exposure, while for others the reverse is true (Sakai et al., 2002). If such a dependency

865   exists for the relevant conditions on Mars, then for sufficiently clean ice, it could enable

866   steepening and runaway growth of a small exposure. A somewhat similar process is

867   observed in models of scalloped depressions, where small disturbances initially cause the

868   bottom of a depression to drop rapidly (Dundas et al., 2015). Antarctic analogs indicate

869   that calving of blocks via thermal expansion-induced cracking may be an important

870   driver of the retreat of steep scarps (e.g., Levy et al., 2013). This has not yet been

871   observed on Mars but is possible, and the scarp faces often appear fractured.

872   In a number of cases, scarps occur in the vicinity of other possible ice-loss

873   landforms and sometimes definitively within the same unit (e.g., Fig. 9). The relationship

874   between the scarp pits and scalloped depressions (e.g., Morgenstern et al., 2007; Soare et

875   al., 2008; Lefort et al., 2009; 2010; Zanetti et al., 2010) is not fully understood, but they

876   appear to form and evolve differently. The major evidence for this difference is that

877   linear ridges are observed parallel to some scarps (Fig. 8), indicating that the scarps

878   retreat in a straight line. Scalloped depressions, by contrast, have arcuate internal ridges

879   (Lefort et al., 2009; Dundas, 2017a). The scarps typically widen as they retreat, resulting

880   in crudely triangular pits that are narrow on the poleward side and widest at the exposed

881   scarp, unlike scalloped depressions (Fig. 9c) and suggesting localized origination.

882   Additionally, the largest scarp pits are commonly multiple kilometers across and occur in

883   relative isolation, while scalloped depressions are typically smaller until mergers create

884   larger complex landforms. Scalloped depressions are commonly interpreted to be

885   sublimation-thermokarst that form via sublimation of an ice-rich unit much like that

886   revealed in the scarps (Morgenstern et al., 2007; Lefort et al., 2009; 2010; Zanetti et al.,

887   2010; Dundas et al., 2015), so one possibility is that they represent different styles of

888   evolution relating to the occurrence of exposed surface ice versus loss through a lag.

889   Poorly defined expanded craters also occur near some scarps. These are interpreted as

890   sublimation-modified impact craters (Dundas et al., 2015; Viola et al., 2015), and the best

891   examples are in Milankovič crater (Fig. 9b). However, while the expanded craters there

892   appear in surface-mantling deposits similar to those hosting the scarps, they are generally

893   not adjacent: the expanded craters are mostly outside the rim of Milankovič, while the

894   scarps are in the crater interior. This could indicate a difference in material properties or

895   surface age, since most of the expanded craters in this region of Mars may be tens of

896   millions of years-old secondary craters (Viola et al., 2015), so the surface-mantling

897   deposits within the crater could be younger. Alternatively, this could indicate a role for

898   the effects of local slope or topography. Near the scarps, irregular pits are more common

899   than either scalloped depressions or expanded craters; given the setting and substrate,

900   these probably also represent ice-loss features.

901   Rather than treating scarps, scalloped depressions, and expanded craters as

902   entirely distinct features, they may be best viewed as the result of different initial

903   conditions and evolutionary pathways for ice-rich deposits affected by sublimation, frost,

904   and wind. Hence, scallop-like landforms arise when disturbances destabilize the surface

905   and cause sublimation through a lag, and expanded craters are fundamentally similar but

906   result from relatively large initial disturbances (impacts) that are not completely erased

907   by sublimation as the crater expands. In cases of strong sublimation, expansion might

908   eventually make the original crater unrecognizable and transition to a scallop-like feature.

909   Both of these morphologies have been effectively modeled via lag-controlled sublimation

910   alone (Dundas et al., 2015; Dundas, 2017a) and retreat should concentrate on the

911   warmest, least-stable slopes. Exposed scarps fit within this framework if they represent a

912   different mode where wind, CO_2 frost, or other factors maintain a bare ice surface which

913   retreats more quickly than ice that is covered by lithic debris, and thus occurs on the

914   slopes where those effects are strongest. The typically straight scarp morphology

915   represents a notable contrast from the other features. Individual landforms could change

916   modes: for instance, a scarp exposure might emerge within a scalloped depression if

917   erosion on the pole-facing slope removes lithic debris, and scarps could become buried if

918   the debris ceases to be removed effectively. The resulting morphologies could be

919   compound features dependent on the initial conditions and variations of the driving forces

920   over time, due both to climate variations and the changing shape of the landform itself.

921   This model raises two important questions. First, under what circumstances do these

922   processes produce well-defined scalloped depressions or expanded craters versus

923   irregular pits? And second, in regions of unstable or marginally stable ice, how much ice

924 is lost to the atmosphere by this localized landform evolution, in comparison with

925 uniform sublimation?

926

927 *5.4. Implications for Martian Climate and Ice Processes*

928   The present-day distribution and properties of ice on Mars record the history of

929 climate, as they reflect an integrated history of deposition, internal processes (such as

930 densification and ice-lens formation), and sublimation. Ice that exists today is either

931 aggrading, stable, or was originally deposited in such abundance that subsequent periods

932 of instability have not been sufficient to remove it. The observations and interpretations

933 above provide some high-level insights about this history.

934   Atmospheric water vapor content is a major control on the distribution of stable

935 ice. If the ice-exposing craters are sampling the upper part of a thick massive ice body in

936 the Arcadia region as discussed above, then the elevated atmospheric water content

937 required to stabilize ice at the lowest-latitude craters (Dundas et al., 2014) might date to

938 the time of deposition or a time-integrated average over subsequent time rather than the

939 most recent climate, since thick ice units can survive over protracted periods while slowly

940 sublimating (e.g., Schorghofer and Forget, 2012; Bramson et al., 2017). If the ice was

941 deposited as snow, that water content would be a lower bound, since surface snow

942 deposition requires more water vapor than subsurface stability. However, the lag

943 developed during retreat must be thinner than predicted by Bramson et al. (2017)

944 assuming nominal conditions for the present day, or the shallow subsurface ice probed by

945 these craters contains excess ice above the deposit indicated by the radar reflectors.

946 Alternative histories for atmospheric water vapor might allow survival with a thinner lag,

947   or sublimation lags may restrict sublimation more than observed in laboratory

948   experiments (Hudson et al., 2007). A generalized latitudinal model by Schorghofer and

949   Forget (2012) does allow lags <1 meter over ice sheets with ages of a few million years

950   or less. The survival time of such ice sheets depends on both the climate history and the

951   time and amount of deposition, as well as the thermophysical properties of the lag itself.

952   As discussed above, scarps may indicate locations of particularly thick, clean ice

953   deposits originating as snow. The apparent high ice content at the scarps suggests that the

954   ratio of ice to dust in the atmosphere was high when deposition was occurring at those

955   locations. Scarps might not exist in all such deposits, and the specific ice bodies hosting

956   scarps may be influenced by local topography. Nevertheless, the scarps likely indicate a

957   subset of favored locations for past ice deposition. Several general circulation model

958   (GCM) studies have examined potential locations of past tropical or mid-latitude snow or

959   frost accumulation under different orbital configurations and axial tilt, with significant

960   differences in the details of model physics as well as in assumptions about H_2O sources

961   and atmospheric dust abundance (e.g., Levrard et al., 2004; Forget et al, 2006; Madeleine

962   et al., 2009; 2014). Due to these differences and the limited sweep of parameter space

963   with any individual model, stating a simple hypothesis that could be tested by comparison

964   with the scarp distribution is not possible at present. Several scenarios do produce

965   concentrated ice accumulation south and southeast of the Hellas basin (hereafter SSE

966   Hellas), which has a marked influence on atmospheric circulation. These include

967   scenarios with low obliquity (15–25°) and an equatorial ice source, particularly with a

968   high optical depth of dust in the atmosphere (Levrard et al., 2004; Madeleine et al.,

969   2009), but also scenarios with 35° obliquity and no equatorial ice source (Madeleine et

970 al., 2014). The seasonal timing of perihelion also strongly affects deposition patterns

971 (Madeleine et al., 2009; 2014). Forget et al. (2006) produced strong deposition east of

972 Hellas, equatorward of the scarps, in a model scenario with 45° obliquity and surface ice

973 at the south polar cap. Scenarios with both low and high obliquity can also produce

974 deposition in the region near Milankovič crater (Madeleine et al., 2009). Other locations

975 of predicted ice deposition in various scenarios do not correspond with scarps, although

976 some match the locations of debris-covered glaciers (e.g., Holt et al., 2008; Plaut et al.,

977 2009; Levy et al., 2014), scalloped depressions (e.g. Morgenstern et al., 2007; Lefort et

978 al., 2009; 2010; Zanetti et al., 2010), or expanded craters (e.g. Viola et al., 2015). The

979 evidence from the scarps favors the past occurrence of one or more of the climate

980 scenarios that produce strong deposition at the scarp locations, and the low dust content

981 of the scarp ice may favor those that produce accumulation with a low optical depth

982 atmosphere. However, Mars' orbital elements have varied widely (e.g., Laskar et al.,

983 2004) and the range of plausible parameters and assumptions makes it difficult to pick

984 out a specific scenario that is unambiguously recorded by the ice.

985   Well-defined meter-scale layering is found in only a few ice-exposing scarps, in

986 contrast with the NPLD where meter- to decameter-scale layering is nearly ubiquitous

987 (e.g., Herkenhoff et al., 2007). Unresolved layers (<30 cm thick) may exist at the mid-

988 latitude scarp sites, preserving a temporal record at small scales, but the more-common

989 crude layering may possibly be the only well-defined time signal in this ice, or the dust

990 content of the ice may be so low or so uniform that layers are mostly not distinguishable

991 in HiRISE images. This could indicate that the ice accumulated only under a narrow

992 range of atmospheric conditions, while polar accumulation occurred in a wider range of

993   climates. However, surface-mantling deposits without ice exposures at latitudes <45° in

994   the mid-latitudes do show evidence of layering (Schon et al., 2009). The two scarp

995   locations with the clearest fine layering both have unconformities and crosscutting layers;

996   this may indicate that accumulation at those sites occurred at two different times possibly

997   with different climates or that some of the deposition occurred as windblown drifts rather

998   than uniform fall deposits. In both cases the uppermost material is approximately

999   horizontal and conforms to the present surface, so it was not affected significantly by

1000   aeolian transport or by ice flow, although deformation could be concentrated out of view

1001   at the base of the ice.

1002   The scarp ice likely records different climate episodes than either of the polar

1003   layered deposits. The available data are too limited to constrain any hypothesis for what

1004   orbital epochs and climate conditions might be recorded in the scarp ice other than to say

1005   that it indicates snow or frost accumulation. Part of this accumulation was likely

1006   geologically recent, since mid-latitude mantling deposits have few craters and young

1007   surface ages of a few million years (Schon et al., 2012), although the base of the deposits

1008   could be older. Harish et al. (2020) estimated the ages of two scarp-hosting craters to be

1009   25 and 95 Ma, and the surface age of one of the host mantling units to be 1 Ma. Viola et

1010   al. (2015) estimated that a mid-latitude icy deposit in the region of Milankovič crater is

1011   tens of millions of years old, and this may include the scarp-hosting ice there, although

1012   the characteristic expanded craters are less abundant in the crater interior, which could be

1013   a younger deposit (Fig. 9b). These ages are less than or comparable to the 30–100 Ma

1014   surface age of the SPLD (e.g., Koutnik et al., 2002), while the entire NPLD may date

1015   from the last several million years (e.g., Levrard et al., 2007; Byrne, 2009; Smith et al.,

1016   2016). More important than the specific age is that deposition in the poles and mid-

1017   latitudes likely occurred under different climate regimes: the locations of net deposition

1018   or loss depend on Mars' obliquity and orbital parameters and associated climate changes

1019   (e.g., Head et al., 2003; Levrard et al., 2004; Forget et al., 2006; Byrne, 2009; Madeleine

1020   et al., 2009; 2014), so polar and mid-latitude ice accumulated at different parts of the

1021   cycle.

1022   Overall, various observations indicate several regions of thick mid-latitude ice

1023   accumulation in the Late Amazonian. These include (1) SSE Hellas, as shown by scarps

1024   and scalloped depressions (Lefort et al., 2010; Zanetti et al., 2010); (2) western Utopia

1025   Planitia, as shown by scalloped depressions and radar reflectors (Morgenstern et al.,

1026   2007; Lefort et al., 2009; Stuurman et al., 2016); and (3) the greater Arcadia region, as

1027   shown by expanded craters and radar reflectors (Viola et al., 2015; Bramson et al., 2015)

1028   and some localized scarps. Debris-covered glaciers also indicate deposition concentrated

1029   east of Hellas, in Tempe Terra, and in the Deuteronilus and Protonilus Mensae regions

1030   (Holt et al., 2008; Plaut et al., 2009; Levy et al., 2014). Note that other major

1031   accumulations could have existed and been subsequently removed, as has occurred for

1032   some lobate debris aprons (Hauber et al., 2008). Deposition was probably not

1033   simultaneous in all of these regions, and the depositional conditions were also probably

1034   variable: ice in debris-covered glaciers and exposed in the scarps likely has a very low

1035   dust content (Campbell and Morgan, 2018; Dundas et al., 2018; Petersen et al., 2018), but

1036   the regional deposits in Utopia and Arcadia may be less ice-rich (Campbell and Morgan,

1037   2018). No site has all of the ice indicators in abundance. Radar reflectors are sparse in

1038   SSE Hellas, although rough topography limits the detectability of possible interfaces in

1039 that region (Cook et al., 2020). Radar loss tangents support high ice contents for debris-

1040 covered glaciers but not for the Utopia and Arcadia deposits. Scarp exposures are sparse

1041 and not found at all in some regions. Additionally, one or the other of scalloped

1042 depressions and expanded craters dominate the sublimation-thermokarst population rather

1043 than a mix occurring. These differences could reflect differences in the lithic content of

1044 the ice (including layering), overburden properties, regional topography (influencing

1045 radar clutter) or the regional climate history.

1046

1047 **6. Conclusions**

1048   We present distributions of ice-exposing craters and large ice-exposing scarps at

1049 middle to high latitudes on Mars. Both types of feature indicate high subsurface ice

1050 contents well in excess of pore filling. Regional variations in the crater exposures suggest

1051 that high ice content is common at shallow depths at mid-latitudes (~40 °N) in the

1052 Arcadia Planitia region compared with the northern part of the Tharsis rise, where pore

1053 ice may be more common. Above ~50° latitude, clean ice exposures are very common at

1054 all longitudes. The nature of ice exposures in some of the largest craters indicates that

1055 clean ice is not a product of the impact process. Variations in crater clusters demonstrate

1056 that both ice content and the depth to ice have substantial local variability. The scarps are

1057 characteristically found between 50–61 °N/S and are concentrated at particular

1058 longitudes. They appear to form in thick surface-mantling deposits produced by past

1059 snowfall and create a distinctive category of sublimation-thermokarst landform. The

1060 latitudinal and longitudinal controls suggest that the scarps form in locations with

1061 particularly thick, clean ice deposits and are exposed by a latitude-dependent process.

1062　Both of these types of exposures provide important constraints on the climate history of

1063　Mars as well as reference locations for other remote-sensing data sets.

1064

1085 and-final-smithed-kernels) via Astropedia and uncontrolled mosaics are included as

1086 layers in JMARS (http://www.mars.asu.edu/data/), which was used for analysis. The

1087 original images used in the mosaics are available via the Planetary Data System Imaging

1088 Node (https://pds-imaging.jpl.nasa.gov/volumes/ody.html). Thermal Emission

1089 Spectrometer (TES) thermal inertia data are available from the PDS Geosciences node

1090 (https://pds-geosciences.wustl.edu/missions/mgs/tes-timap.html) and albedo data at the

1091 PDS TES data node (http://tes.asu.edu/products/index.html). The use of trade, product, or

1092 firm names is for identification purposes only and does not constitute an endorsement by

1093 the U.S. Government.

1094

1095 **References**

1096 Appéré, T., Schmitt, B., Langevin, Y., Douté, S., Pommerol, A., Forget, F., Spiga, A.,

1097   Gondet, B., Bibring, J.-P. (2011). Winter and spring evolution of northern seasonal

1098   deposits on Mars from OMEGA on Mars Express. *J. Geophys. Res., 115,* E05001.

1099   https://doi.org/10.1029/2010JE003762.

1100 Aylward, D. S., Schmidt, L. M., Levy, J. S. (2019). Formation of coarse sediment lags in

1101   ice-sediment mixtures: A geomorphic signature of sublimation on regolith surfaces.

1102   *Planet. Space Sci.*, 174, 8-13. https://doi/org/10.1016/j.pss.2019.05.006.

1103 Bandfield, J. L. (2007). High-resolution subsurface water-ice distributions on Mars.

1104   *Nature, 447,* 64-67. https://doi.org/10.1038/nature05781.

1105 Bandfield, J. L., & Feldman, W. C. (2008). Martian high-latitude permafrost depth and

1106   surface cover thermal inertia distributions. *J. Geophys. Res., 113,* E08001.

1107   https://doi.org/10.1029/2007JE003007.

1108   Bart, G. D. (2014). The quantitative relationship between small impact crater morphology

1109   and regolith depth. *Icarus, 235,* 130-135.

1110   https://doi.org/10.1016/j.icarus.2014.03.020.

1111   Boynton, W. V., Feldman, W. C., Squyres, S. W., Prettyman, T. H., Brückner, J., Evans,

1112   L. G., et al. (2002). Distribution of hydrogen in the near surface of Mars: Evidence

1113   for subsurface ice deposits. *Science, 297,* 81-85.

1114   https://doi.org/10.1126/science.1073722.

1115   Bramson, A. M., Byrne, S., Putzig, N. E., Sutton, S., Plaut, J. J., Brothers, T. C., & Holt,

1116   J. W. (2015). Widespread excess ice in Arcadia Planitia, Mars. *Geophys. Res. Lett.,*

1117   *42,* 6566-6574. https://doi.org/10.1002/2015GL064844.

1118   Bramson, A. M., Byrne, S., Bapst, J. (2017). Preservation of mid-latitude ice sheets on

1119   Mars. *J. Geophys. Res., 122*, 2,250-2,266. https://doi.org/10.1002/2017JE005357.

1120   Bramson, A. M., Byrne, S., Bapst, J., Smith, I. B., McClintock, T. (2019). A migration

1121   model for the polar spiral troughs of Mars. *J. Geophys. Res.*, *124*, 1,020-1,043.

1122   https://doi.org/10.1029/2018JE005806.

1123   Bridges, N. T., et al. (2010). Aeolian bedforms, yardangs, and indurated surfaces in the

1124   Tharsis Montes as seen by the HiRISE camera: Evidence for dust aggregates. *Icarus*,

1125   *205*, 165-182. https://doi.org/10.1016/j.icarus.2009.05.017.

1126   Buri, P., Pellicciotti, F. (2018). Aspect controls the survival of ice cliffs on debris-

1127   covered glaciers. *Proc. Nat. Acad. Sci., 115,* 4,369-4,374.

1128   https://doi.org/10.1073/pnas.1713892115.

1129   Byrne, S. (2009). The polar deposits of Mars. *Ann. Rev. Earth Planet. Sci., 37,* 535-560.

1130   https://doi.org/10.1146/annurev.earth.031208.100101.

1131 Byrne, S., Dundas, C. M., Kennedy, M. R., Mellon, M. T., McEwen, A. S., Cull, S. C., et

1132   al. (2009). Distribution of mid-latitude ground ice on Mars from new impact craters.

1133   *Science*, *325,* 1674-1676. https://doi.org/10.1126/science.1175307.

1134 Campbell, B. A., Morgan, G. A. (2018). Fine-scale layering of Mars polar deposits and

1135   signatures of ice content in nonpolar material from multiband SHARAD data

1136   processing. *Geophys. Res. Lett., 45,* 1,759-1,766.

1137   https://doi.org/10.1002/2017GL075844.

1138 Chamberlain, M. A., & Boynton, W. V. (2007). Response of Martian ground ice to orbit-

1139   induced climate change. *J. Geophys. Res., 112,* E06009.

1140   https://doi.org/10.1029/2006JE002801.

1141 Christensen, P. R., Bandfield, J. L., Hamilton, V. E., Ruff, S. W., Kieffer, H. H., et al.

1142   (2001). Mars Global Surveyor Thermal Emission Spectrometer experiment:

1143   Investigation description and surface science results. *J. Geophys. Res., 106,* 23,823-

1144   23,871. https://doi.org/10.1029/2000JE001370.

1145 Christensen, P. R., Jakosky, B. M., Kieffer, H. H., Malin, M. C., McSween, H. Y. Jr.,

1146   Nealson, K., et al. (2004). The Thermal Emission Imaging System (THEMIS) for the

1147   Mars 2001 Odyssey mission. *Space Sci. Rev., 110*(1), 85-130.

1148   https://doi.org/10.1023/B:SPAC.0000021008.16305.94.

1149 Clark, R. N., & Lucey, P. G. (1984). Spectral properties of ice-particulate mixtures and

1150   implications for remote sensing. 1. Intimate mixtures. *J. Geophys. Res., 89,* 6,341-

1151   6,348. https://doi.org/10.1029/JB089iB07p06341.

1152 Conway, S. J., & Balme, M. R. (2014). Decameter thick remnant glacial ice deposits on

1153   Mars. *Geophys. Res. Lett.*, *41,* 5402-5409. https://doi.org/10.1002/2014GL060314.

Cook, C. W., Bramson, A. M., Byrne, S., Holt, J. W., Christoffersen, M. S., Viola, D.,

Dundas, C. M., Goudge, T. A. (2020). Sparse subsurface radar reflectors in Hellas

Planitia, Mars. *Icarus*, *348*, article #113847.

https://doi.org/10.1016/j.icarus.2020.113847.

Cull, S., Arvidson, R. E., Mellon, M. T., Skemer, P., Shaw, A., Morris, R. V. (2010).

Composition of subsurface ices at the Mars Phoenix landing site. *Geophys. Res. Lett.,*

37, L24203. https://doi.org/10.1029/2010GL045372.

Delamere, W. A., et al. (2010). Color imaging of Mars by the High Resolution Imaging

Science Experiment (HiRISE). *Icarus, 205,* 38-52.

https://doi.org/10.1016/j.icarus.2009.03.012.

Dundas, C. M. (2017a). Effects of varying obliquity on Martian sublimation thermokarst

landforms. *Icarus, 281*, 115-120. https://doi.org/10.1016/j.icarus.2016.08.031.

Dundas, C. M. (2017b). Effects of lava heating on volatile-rich slopes on Io. *J. Geophys.*

Res. Planets, 122, 546-559. https://doi.org/10.1002/2016JE005177.

Dundas, C. M., Byrne, S., McEwen, A. S., Mellon, M. T., Kennedy, M. R., Daubar, I. J.,

Saper, L. (2014). HiRISE observations of new impact craters exposing Martian

ground ice. *J. Geophys. Res., 119,* 109-127. https://doi.org/10.1002/2013JE004482.

Dundas, C. M., Byrne, S., & McEwen, A. S. (2015). Modeling the development of

Martian sublimation thermokarst landforms. *Icarus*, *262*, 154-169.

https://doi.org/10.1016/j.icarus.2015.07.033.

Dundas, C. M., Bramson, A. M., Ojha, L., Wray, J. J., Mellon, M. T., Byrne, S., et al.

(2018). Exposed subsurface ice sheets in the Martian mid-latitudes. *Science, 359*,

199-201. https://doi.org/10.1126/science.aao1619.

1177   Dundas, C. M., McEwen, A. S., Diniega, S., Hansen, C. J., Byrne, S., McElwaine, J. N.

1178   (2019). The formation of gullies on Mars today. *Geol. Soc. London Spec. Pub., 467*,

1179   67-94. https://doi.org/10.1144/SP467.5.

1180   Dundas, C. M., Mellon, M. T., Conway, S. J., Daubar, I. J., Williams, K. E., Ojha, L.,

1181   Wray, J. J., Bramson, A. M., Byrne, S., McEwen, A. S., Posiolova, L. V., Speth, G.,

1182   Viola, D., Landis, M., Morgan, G. A., and Pathare, A. V. (2021). Supplementary Data

1183   for "Widespread Exposures of Extensive Clean Shallow Ice in the Mid-Latitudes of

1184   Mars": U.S. Geological Survey data release. https://doi.org/10.5066/P9Y8FR1R.

1185   Fassett, C. I., Levy, J. S., Dickson, J. L., & Head, J. W. (2014). An extended period of

1186   episodic northern mid-latitude glaciation on Mars during the Middle to Late

1187   Amazonian: Implications for long-term obliquity history. *Geology*, *42*, 763-766.

1188   https://doi.org/10.1130/G35798.1.

1189   Fergason, R. L., & Weller, L. (2019). The THEMIS controlled mosaics of Mars and final

1190   smithed kernels. 4th Planetary Data Workshop, abstract #7059.

1191   Fischer, E. M., & Pieters, C. M. (1993). The continuum slope of Mars: Bidirectional

1192   reflectance investigations and applications to Olympus Mons. *Icarus, 102,* 185-202.

1193   https://doi.org/10.1006/icar.1993.1043.

1194   Fisher, D. A. (2005). A process to make massive ice in the Martian regolith using long-

1195   term diffusion and thermal cracking. *Icarus*, *179,* 387-397.

1196   https://doi.org/10.1016/j.icarus.2005.07.024.

1197   Forget, F., Haberle, R. M., Montmessin, F., Levrard, B., Head, J. W. (2006). Formation

1198   of glaciers on Mars by atmospheric precipitation at high obliquity. *Science, 311*, 368-

1199   371. https://doi.org/10.1126/science.1120335.

1200 Geissler, P. E. (2014). The birth and death of transverse aeolian ridges on Mars. *J.*

1201   *Geophys. Res., 119*, 2583-2599. https://doi.org/10.1002.2014JE004633.

1202 Haltigin, T., Osinski, G., Baylis, A., Barnard, I. (2018). Orbital Synthetic Aperture Radar

1203   for subsurface ice detection on Mars: Scientific rationale and Canadian technical

1204   concept. 42nd COSPAR Scientific Assembly, abstract B4.2-33-18.

1205 Harish, Vijayan, S., Mangold, N., Bhardwaj, A. (2020). Water-ice exposing scarps within

1206   the northern mid-latitude craters on Mars. *Geophys. Res. Lett.*, 47, e2020GL089057.

1207   https://doi.org/10.1029/2020GL089057.

1208 Hauber, E., van Gasselt, S., Chapman, M. G., Neukum, G. (2008). Geomorphic evidence

1209   for former lobate debris aprons at low latitudes on Mars: Indicators of the Martian

1210   paleoclimate. *J. Geophys. Res., 113*, E02007. https://doi.org/10.1029/2007JE002897.

1211 Head, J. W., Mustard, J. F., Kreslavsky, M. A., Milliken, R. E., Marchant, D. R. (2003).

1212   Recent ice ages on Mars. *Nature, 426,* 797-802. https://doi.org/10.1038/nature02114.

1213 Heldmann, J. L., Schurmeier, L., McKay, C., Davila, A., Stoker, C., Marinova, M.,

1214   Wilhelm, M. B. (2014). Midlatitude ice-rich ground on Mars as a target in the search

1215   for evidence of life and for *in situ* resource utilization on human missions.

1216   *Astrobiology, 14,* 102-118. https://doi.org/10.1089/ast.2013.1103.

1217 Herkenhoff, K. E., Byrne, S., Russell, P. S., Fishbaugh, K. E., & McEwen, A. S. (2007).

1218   Meter-scale morphology of the north polar region of Mars. *Science, 317,* 1711-1715.

1219   https://doi.org/10.1126/science.1143544.

1220 Holt, J. W., et al. (2008). Radar sounding evidence for buried glaciers in the southern

1221   mid-latitudes of Mars. *Science, 322,* 1,235-1,238.

1222   https://doi.org/10.1126/science.1164246.

1223 Hudson, T. L., Aharonson, O., Schorghofer, N., Farmer, C. B., Hecht, M. H., Bridges, N.

1224   T. (2007). Water vapor diffusion in Mars subsurface environments. *J. Geophys. Res.,*

1225   *112*, E05016. https://doi.org/10.1029/2006JE002815.

1226 Hudson, T. L., Aharonson, O. (2008). Diffusion barriers at Mars surface conditions: Salt

1227   crusts, particle size mixtures, and dust. *J. Geophys. Res., 113,* E09008.

1228   https://doi.org/10.1029/2007JE003026.

1229 Kerrigan, M. (2013). The periglacial landscape of Utopia Planitia: Geologic evidence for

1230   recent climate change on Mars. MS thesis, Dept. of Earth Sciences, Univ. Western

1231   Ontario, London, Ontario, Canada.

1232 Khuller, A. R., & Christensen, P. R. (2019). Evidence of water-rich snow deposits within

1233   Martian gullies. Lunar Planet. Sci. Conf. 50, abstract #3060.

1234 Kieffer, H. H. (2007). Cold jets in the Martian polar caps. *J. Geophys. Res., 112,* E08005.

1235   https://doi.org/10.1029/2006JE002816.

1236 Kirkbride, M. P. (1993). The temporal significance of transitions from melting to calving

1237   termini at glaciers in the central Southern Alps of New Zealand. *The Holocene, 3,*

1238   232-240. https://doi.org/10.1177/095968369300300305.

1239 Koutnik, M., Byrne, S., Murray, B. (2002). *J. Geophys. Res. Planets,* 107, E11, 5100.

1240   https://doi.org/10.1029/2001JE001805.

1241 Landis, M., McEwen, A. S., Daubar, I. J., Hayne, P. O., Byrne, S., Dundas, C. M.,

1242   Sutton, S. S., Britton, A., Herkenhoff, K. E. (2020). South Polar Layered Deposits

1243   near-surface properties inferred from a dated impact crater. 7th Int. Conf. Mars Polar

1244   Sci. Expl., abstract #6025.

1245   Laskar, J., Correia, A. C. M., Gastineau, M., Joutel, F., & Levrard, B. (2004). Long term

1246   evolution and chaotic diffusion of the insolation quantities of Mars. *Icarus, 170*, 343-

1247   364. https://doi.org/10.1016/j.icarus.2004.04.005.

1248   Lefort, A., Russell, P. S., Thomas, N., McEwen, A. S., Dundas, C. M., & Kirk, R. L.

1249   (2009). Observations of periglacial landforms in Utopia Planitia with the High

1250   Resolution Imaging Science Experiment (HiRISE). *J. Geophys. Res., 114,* E04005.

1251   https://doi.org/10.1029/2008JE003264.

1252   Lefort, A., Russell, P. S., & Thomas, N. (2010). Scalloped terrains in the Peneus and

1253   Amphitrites Paterae region of Mars as observed by HiRISE. *Icarus, 205,* 259-268.

1254   https://doi.org/10.1016/j.icarus.2009.06.005.

1255   Leighton, R. B., & Murray, B. C. (1966). Behavior of carbon dioxide and other volatiles

1256   on Mars. *Science, 153*, 136-144. https://doi.org/10.1126/science.153.3732.136.

1257   Levrard, B., Forget, F., Montmessin, F., Laskar, J. (2004). Recent ice-rich deposits

1258   formed at high latitudes on Mars by sublimation of unstable equatorial ice during low

1259   obliquity. *Nature, 431*, 1,072-1,075. https://doi.org/10.1038/nature03055.

1260   Levrard, B., Forget, F., Montmessin, F., Laskar, J. (2007). Recent formation and

1261   evolution of northern Martian polar layered deposits as inferred from a global climate

1262   model. *J. Geophys. Res., 112*, E06012. https://doi.org/10.1029/2006JE002772.

1263   Levy, J. S., Head, J., Marchant, D. (2009a). Thermal contraction crack polygons on Mars:

1264   Classification, distribution, and climate implications from HiRISE observations. *J.*

1265   *Geophys. Res., 114,* E01007. https://doi.org/10.1029/2008JE003273.

1266 Levy, J. S., Head, J., Marchant, D. (2009b). Concentric crater fill in Utopia Planitia:

1267   History and interaction between glacial "brain terrain" and periglacial mantle

1268   processes. *Icarus, 202,* 462-476. https://doi.org/10.1016/j.icarus.2009.02.018.

1269 Levy, J. S., Fountain, A. G., Dickson, J. L., Head, J. W., Okal, M., Marchant, D. R.,

1270   Watters, J. (2013). Accelerated thermokarst formation in the McMurdo Dry Valleys,

1271   Antarctica. *Sci. Rep., 3,* 2269. https://doi.org/10.1038/srep02269.

1272 Levy, J. S., Fassett, C. I., Head, J. W., Schwartz, C., Watters, J. L. (2014). Sequestered

1273   ice contribution to the global Martian water budget: Geometric constraints on the

1274   volume of remnant, midlatitude debris-covered glaciers. *J. Geophys. Res.*, *119*, 2,188-

1275   2,196. https://doi.org/10.1002/2014JE004685.

1276 Madeleine, J.-B., Forget, F., Head, J. W., Levrard, B., Montmessin, F., Millour, E.

1277   (2009). Amazonian northern mid-latitude glaciation on Mars: A proposed climate

1278   scenario. *Icarus, 203,* 390-405. https://doi.org/10.1016/j.icarus.2009.04.037.

1279 Madeleine, J.-B., Head, J. W., Forget, F., Navarro, T., Millour, E., Spiga, A., Colaïtis, A.,

1280   Määttänen, A., Montmessin, F., & Dickson, J. L. (2014). Recent Ice Ages on Mars:

1281   The role of radiatively active clouds and cloud microphysics. *Geophys. Res. Lett., 41,*

1282   4873-4879. https://doi.org/10.1002/2014GL059861.

1283 Malin, M. C., Bell, J. F., Cantor, B. A., Caplinger, M. A., Calvin, W. M., et al. (2007).

1284   Context Camera investigation on board the Mars Reconnaissance Orbiter. *J. Geophys.*

1285   *Res., 112*, E05S04. https://doi.org/10.1029/2006JE002808.

1286 Mangold, N. (2005). High latitude patterned grounds on Mars: Classification, distribution

1287   and climatic control. *Icarus, 174,* 336-359.

1288   https://doi.org/10.1016/j.icarus.2004.07.030.

1289   McEwen, A. S., Eliason, E. M., Bergstrom, J. W., Bridges, N. T., Hansen, C. J., et al.

1290   (2007). Mars Reconnaissance Orbiter's High Resolution Imaging Science

1291   Experiment. *J. Geophys. Res.*, *112*, E05S02. https://doi.org/10.1029/2005JE002605.

1292   Mellon, M. T. (1997). Small-scale polygonal features on Mars: Seasonal thermal

1293   contraction cracks in permafrost. *J. Geophys. Res., 102,* 25,617-25,628.

1294   https://doi.org/10.1029/97JE02582.

1295   Mellon, M. T., & Jakosky, B. M. (1993). Geographic variations in the thermal and

1296   diffusive stability of ground ice on Mars. *J. Geophys. Res.*, *98*, 3345-3364.

1297   https://doi.org/10.1029/92JE02355.

1298   Mellon, M. T., & Jakosky, B. M. (1995). The distribution and behavior of Martian

1299   ground ice during past and present epochs. *J. Geophys. Res.*, *100,* 11,781-11,799.

1300   https://doi.org/10.1029/95JE01027.

1301   Mellon, M. T., Feldman, W. C., & Prettyman, T. H. (2004). The presence and stability of

1302   ground ice in the southern hemisphere of Mars. *Icarus, 169,* 324-340.

1303   https://doi.org/10.1016/j.icarus.2003.10.022.

1304   Mellon, M. T., Arvidson, R. E., Sizemore, H. G., Searls, M. L., Blaney, D. L., Cull, S., et

1305   al. (2009). Ground ice at the Phoenix landing site: Stability state and origin. *J.*

1306   *Geophys. Res., 114,* E00E07. https://doi.org/10.1029/2009JE003417.

1307   Melosh, H. J. (1989). Impact Cratering: A Geologic Process. New York: Oxford

1308   University Press.

1309   MEPAG ICE-SAG Report (2019). Report from the Ice and Climate Evolution Science

1310   Analysis Group (ICE-SAG). S. Diniega and N. E. Putzig (chairs), 157 pages posted 8

1311   July 2019 by the Mars Exploration Program Analysis Group (MEPAG) at

1312   http://mepag.nasa.gov/reports.cfm.

1313   Milliken, R. A., Mustard, J. F., & Goldsby, D. L. (2003). Viscous flow features on the

1314   surface of Mars: Observations from high-resolution Mars Orbiter Camera (MOC)

1315   images. *J. Geophys. Res., 108,* 5057. https://doi.org/10.1029/2002JE002005.

1316   Mitrofanov, I. G., Malakhov, A. V., Golovin, D. V., Litvak, M. L., Sanin, A. B.,

1317   Mokrousov, M. I. (2018). Neutron mapping of Mars with high spatial resolution: First

1318   results of the FREND experiment of the ExoMars project. Proceedings of the Russian

1319   Academy of Science, the Branch of Physical Science.

1320   Morgan, G. A., et al. (2020). Subsurface water ice mapping (SWIM) on Mars: Radar

1321   surface reflectivity. Lunar Planet. Sci. Conf. 51, abstract #2790.

1322   Morgenstern, A., Hauber, E., Reiss, D., van Gasselt, S., Grosse, G., Schirrmeister, L.

1323   (2007). Deposition and degradation of a volatile-rich later in Utopia Planitia and

1324   implications for climate history on Mars. *J. Geophys. Res., 112,* E06010.

1325   https://doi.org/10.1029/2006JE002869.

1326   Mouginot, J., Pommerol, A., Kofman, W., Beck, P., Schmitt, B., Herique, A., Grima, C.,

1327   Safaeinili, A., & Plaut, J. J. (2010). The 3-5 MHz global reflectivity map of Mars by

1328   MARSIS/Mars Express: Implications for the current inventory of subsurface H_2O.

1329   *Icarus, 210,* 612-625. https://doi.org/10.1016/j.icarus.2010.07.003.

1330   Murray, B. C., Ward, W. R., & Yeung, S. C. (1973). Periodic insolation variations on

1331   Mars. *Science, 180*, 638-640. https://doi.org/10.1126/science.180.4086.638.

1332 Mustard, J. F., Cooper, C. D., Rifkin, M. K. (2001). Evidence for recent climate change

1333   on Mars from the identification of youthful near-surface ground ice. *Nature, 412,*

1334   411-414. https://doi.org/10.1038/35086515.

1335 Noe Dobrea, E. Z., Asphaug, E., Grant, J. A., Kessler, M. A., Mellon, M. T. (2007).

1336   Patterned ground as an alternative explanation for the formation of brain coral

1337   textures in the mid latitudes of Mars: HiRISE observations of lineated valley fill

1338   textures. 7th Int. Conf. Mars, abstract #3358.

1339 Orloff, T. C., Kreslavsky, M. A., Asphaug, E. I. (2013). Possible mechanism of boulder

1340   clustering on Mars. *Icarus, 225,* 992-999.

1341   https://doi.org/10.1016/j.icarus.2013.01.002.

1342 Pathare, A. V., Feldman, W. C., Prettyman, T. H., & Maurice, S. (2018). Driven by

1343   excess? Climatic implications of new global mapping of near-surface water-

1344   equivalent hydrogen on Mars. *Icarus, 301,* 97-116.

1345   https://doi.org/10.1016/j.icarus.2017.09.031.

1346 Petersen, E. I., Holt, J. W., & Levy, J. S. (2018). High ice purity of Martian lobate debris

1347   aprons at the regional scale: Evidence from an orbital radar sounding survey in

1348   Deuteronilus and Protonilus Mensae. *Geophys. Res. Lett., 45,* 11,595-11,604.

1349   https://doi.org/10.1029/2018GL079759.

1350 Picardi, G., et al. (2005). Radar soundings of the subsurface of Mars. *Science, 310,* 1,925-

1351   1,928. https://doi.org/10.1126/science.1122165.

1352 Pilorget, C., & Forget, F. (2016). Formation of gullies on Mars by debris flows triggered

1353   by CO_2 sublimation. *Nature Geosci., 9,* 65-69. https://doi.org/10.1038/NGEO2619.

1354   Piqueux, S., Buz, J., Edwards, C. S., Bandfield, J. L., Kleinböhl, A., Kass, D. M., Hayne,

1355   P. O., & the MCS and THEMIS teams (2019). Widespread shallow water ice on Mars

1356   at high latitudes and mid latitudes. *Geophys. Res. Lett., 46,* 14,290-14,298.

1357   https://doi.org/10.1029/2019GL083947.

1358   Plaut, J. J., et al. (2007). Subsurface radar sounding of the south polar layered deposits of

1359   Mars. *Science, 316,* 92-95. https://doi.org/10.1126/science.1139672.

1360   Plaut, J. J., Safaeinili, A., Holt, J. W., Phillips, R. J., Head, J. W., Seu, R., Putzig, N. E.,

1361   & Frigeri, A. (2009). Radar evidence for ice in lobate debris aprons in the mid-

1362   northern latitudes of Mars. *Geophys. Res. Lett., 36,* L02203.

1363   https://doi.org/10.1029/2008GL036379.

1364   Putzig, N. E., & Mellon, M. T. (2007). Apparent thermal inertia and the surface

1365   heterogeneity of Mars. *Icarus, 191,* 68-94.

1366   https://doi.org/10.1016/j.icarus.2007.05.013.

1367   Putzig, N. E., et al. (2019). Results of the Mars Subsurface Water Ice Mapping (SWIM)

1368   project. 9th Int. Mars Conference, abstract #6427.

1369   Putzig, N. E., et al. (2020). Subsurface Water Ice Mapping (SWIM) on Mars to support in

1370   situ resource utilization. Lunar and Planetary Science Conference 51, abstract #2648.

1371   Quaide, W. L., Oberbeck, V. R. (1968). Thickness determination of the lunar surface

1372   layer from lunar impact craters. *J. Geophys. Res., 73,* 5,247-5,270.

1373   https://doi.org/10.1029/JB073i016p05247.

1374   Reufer, A., Thomas, N., Benz, W., Byrne, S., Bray, V., Dundas, C., & Searls, M. (2010).

1375   Models of high velocity impacts into dust-covered ice: Application to Martian

northern lowlands. *Planet. Space Sci.*, *58,* 1160-1168.
https://doi.org/10.1016/j.pss.2010.04.008.

Rice, M. S., Bell, J. F., Cloutis, E. A., Wray, J. J., Herkenhoff, K. E., Sullivan, R.,
Johnson, J. R., & Anderson, R. B. (2011). Temporal observations of bright soil
exposures at Gusev crater, Mars. *J. Geophys. Res., 116,* E00F14.
https://doi.org/10.1029/2010JE003683.

Ruff, S. W., & Christensen, P. R. (2002). Bright and dark regions on Mars: Particle size
and mineralogical characteristics based on Thermal Emission Spectrometer data. *J.
Geophys. Res., 107,* E12, 5127. https://doi.org/10.1029/2001JE001580.

Russell, P., et al. (2008). Seasonally active frost-dust avalanches on a north polar scarp of
Mars captured by HiRISE. *Geophys. Res. Lett., 35,* L23204.
https://doi.org/10.1029/2008GL035790.

Sakai, A., Nakawo, M., Fujita, K. (2002). Distribution characteristics and energy balance
of ice cliffs on debris-covered glaciers, Nepal Himalaya. *Arctic, Antarctic and Alpine
Research, 34,* 12-19. https://doi.org/10.1080/15230430.2002.12003463.

Schon, S. C., Head, J. W., Milliken, R. E. (2009). A recent ice age on Mars: Evidence for
climate oscillations from regional layering in mid-latitude mantling deposits.
Geophys. Res. Lett., 36, L15202. https://doi.org/10.1029/2009GL038554.

Schon, S. C., Head, J. W., Fassett, C. I. (2012). Recent high-latitude resurfacing by a
climate-related latitude-dependent mantle: Constraining age of emplacement from
counts of small craters. *Planet. Space Sci.*, *69*, 49-61.
https://doi.org/10.1016/j.pss.2012.03.015.

1398   Schorghofer, N., & Aharonson, O. (2005). Stability and exchange of subsurface ice on

1399   Mars. *J. Geophys. Res., 110,* E05003. https://doi.org/10.1029/2004JE002350.

1400   Schorghofer, N., & Forget, F. (2012). History and anatomy of subsurface ice on Mars.

1401   *Icarus, 220,* 1112-1120. https://doi.org/10.1016/j.icarus.2012.07.003.

1402   Sizemore, H. G., & Mellon, M. T. (2006). Effects of soil heterogeneity on Martian

1403   ground-ice stability and orbital estimates of ice table depth. *Icarus*, *185*, 358-369.

1404   https://doi.org/10.1016/j.icarus.2006.07.018.

1405   Sizemore, H. G., Zent, A. P., & Rempel, A. W. (2015). Initiation and growth of Martian

1406   ice lenses. *Icarus, 251,* 191-210. https://doi.org/10.1016/j.icarus.2014.04.013.

1407   Smith, I. B., Putzig, N. E., Holt, J. W., Phillips, R. J. (2016). An ice age recorded in the

1408   polar deposits of Mars. *Science*, *352*, 1075-1079.

1409   https://doi.org/10.1126/science.aad6968.

1410   Smith, I. B., Diniega, S., Beaty, D. W., Thorsteinsson, T., Becerra, P., Bramson, A. M., et

1411   al. (2018). 6th International Conference on Mars Polar Science and Exploration:

1412   Conference summary and five top questions. *Icarus, 308,* 2-14.

1413   https://doi.org/10.1016/j.icarus.2017.06.027.

1414   Smith, P. H., Tamppari, L. K., Arvidson, R. E., Bass, D., Blaney, D., Boynton, W. V., et

1415   al. (2009). H_2O at the Phoenix landing site. *Science, 325,* 58-61.

1416   https://doi.org/10.1126/science.1172339.

1417   Soare, R. J., Osinski, G. R., Roehm, C. L. (2008). Thermokarst lakes and ponds on Mars

1418   in the very recent (Late Amazonian) past. *Earth Planet. Sci. Lett., 272,* 382-393.

1419   https://doi.org/10.1016/j.epsl.2008.05.010.

1420   Soderblom, L. A., Kreidler, T. J., Masursky, H. (1973). Latitudinal distribution of a

1421   debris mantle on the Martian surface. *J. Geophys. Res., 78,* 4,117-4,122.

1422   https://doi.org/10.1029/JB078i020p04117.

1423   Squyres, S. W. (1978). Martian fretted terrain: Flow of erosional debris. *Icarus, 34,* 600-

1424   613. https://doi.org/10.1016/0019-5(78)90048-9.

1425   Squyres, S. W., Carr, M. H. (1986). Geomorphic evidence for the distribution of ground

1426   ice on Mars. *Science, 231,* 249-252. https://doi.org/10.1126/science.231.4735.249.

1427   Steele, L. J., Balme, M. R., & Lewis, S. R. (2017). Regolith-atmosphere exchange of

1428   water in Mars' recent past. *Icarus, 284,* 233-248.

1429   https://doi.org/10.1016/j.icarus.2016.11.023.

1430   Stuurman, C. M., Osinski, G. R., Holt, J. W., Levy, J. S., Brothers, T. C., Kerrigan, M., &

1431   Campbell, B. A. (2016). SHARAD detection and characterization of subsurface water

1432   ice deposits in Utopia Planitia, Mars. *Geophys. Res. Lett., 43,* 9484-9491,

1433   https://doi.org/10.1002/2016GL070138.

1434   van Everdingen, R. O., ed. (1998, revised 2005). Multi-language glossary of permafrost

1435   and related ground-ice terms. International Permafrost Association, 159 pages.

1436   Vincendon, M., Forget, F., Mustard, J. (2010). Water ice at low to midlatitudes on Mars.

1437   *J. Geophys. Res.*, *115*, E10001. https://doi.org/10.1029/2010JE003584.

1438   Viola, D., McEwen, A. S. (2018). Geomorphological evidence for shallow ice in the

1439   southern hemisphere of Mars. *Geophys. Res. Lett, 123,* 262-277.

1440   https://doi.org/10.1002/2017JE005366.

1441   Viola, D., McEwen, A. S., Dundas, C. M., & Byrne, S. (2015). Expanded secondary

1442   craters in the Arcadia Planitia region, Mars: Evidence for tens of Myr-old shallow

1443   subsurface ice. *Icarus, 248,* 190-204. https://doi.org/10.1016/j.icarus.2014.10.032.

1444   Ward, W. R. (1973). Large-scale variations in the obliquity of Mars. *Science*, *181*, 260-

1445   262. https://doi.org/10.1126/science.181.4096.260.

1446   Wells, E. N., Veverka, J., & Thomas, P. (1984). Mars: Experimental study of albedo

1447   changes caused by dust fallout. *Icarus*, *58*, 331-338. https://doi.org/10.1016/0019-

1448   1035(84)90079-4.

1449   Zanetti, M., Hiesinger, H., Reiss, D., Hauber, E., & Neukum, G. (2010). Distribution and

1450   evolution of scalloped terrain in the southern hemisphere, Mars. *Icarus, 206*, 691-706.

1451   https://doi.org/10.1016/j.icarus.2009.09.010.

1452   Zuber, M. T., Phillips, R. J., Andrews-Hanna, J. C., Asmar, S. W., Konopliv, A. S.,

1453   Lemoine, F. G., Plaut, J. J., Smith, D. E., & Smrekar, S. E. (2007). Density of Mars'

1454   south polar layered deposits. *Science, 317,* 1718-1719.

1455   https://doi.org/10.1126/science.1146995.

1456

1457 **Table 1. Depths to Strong Layer at Impact Sites with Icy Color**

Latitude	Longitude	N	Mean depth to ice (m)	Range
46.35°	176.89°	6	0.42	0.28 – 0.58
44.22°	164.20°	5	0.47	0.26 – 0.55
50.51°	265.2°	3	0.42	0.32 – 0.62
39.11°	190.25°	2	0.90	0.69 – 1.1
47.43°	112.01°	2	0.50	0.40 – 0.60

1458 Planetocentric latitude, east longitude. N is the number of craters with morphologies

1459 indicating weak-over-strong layering, which are not necessarily those with visible ice.

1460 Values are given to two significant figures for relative comparison but for typical crater

1461 sizes, the potential measurement error on an individual crater is ±~30% assuming half-

1462 pixel errors in opposite directions for the rim and floor diameter. The range is the spread

1463 between the largest and smallest measurements and does not include measurement

1464 uncertainty.

1465

1466 **Figures and Captions**
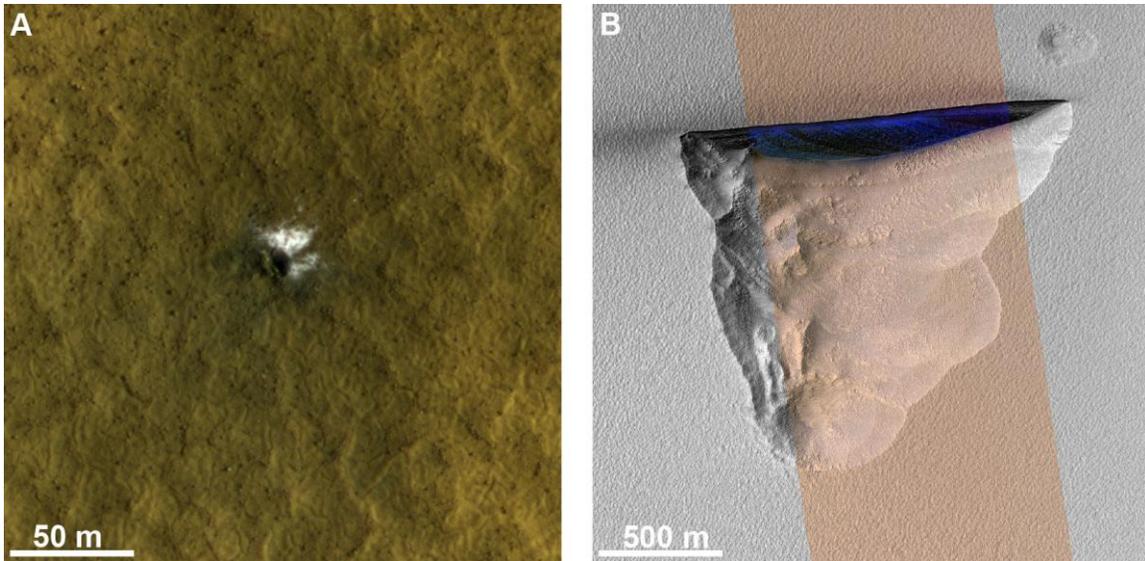
1467

Figure 1. A) Example of an ice-exposing crater (69.3 °N, 142.2 °E). Note patchy, bright,

relatively white ejecta, suggesting that this crater excavated both regolith and clean ice,

as well as polygonal patterns consistent with thermal contraction cracks. B) Southern

hemisphere ice-exposing scarp #6 (56.9 °S, 96.3 °E). Note distinct relatively blue

coloration confined to the scarp face, which is approximately straight, sharp-edged, and

faces the pole. (A: HiRISE image ESP_046189_2495, acquired at L_S=163°. Illumination

is from the right and north is to the lower left (polar stereographic projection). B: HiRISE

image ESP_057466_1230, acquired at L_S=279°. Illumination is from the upper left and

north is up. All image figures herein are map projected in equirectangular projection with

north up unless otherwise noted, and colors are enhanced as described in the text.)
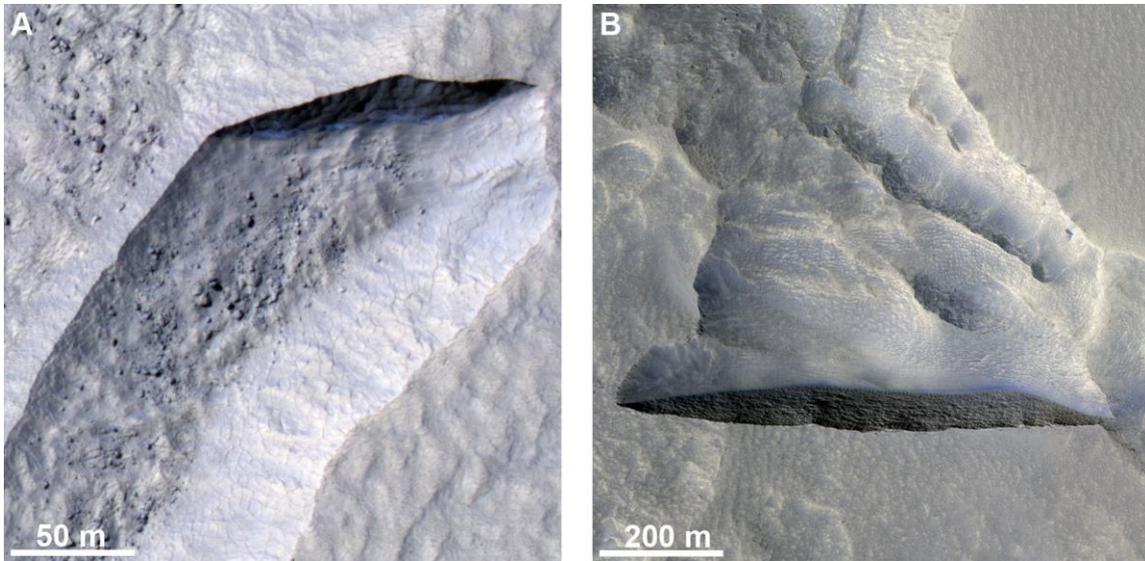
1478

Figure 2. A) Example of a confirmed but marginal icy scarp (southern hemisphere scarp #13), where there is weak coloration of relatively blue material confined to only portions of the scarp face. B) Example of a scarp that has the morphology of an ice exposure but lacks the coloration. These are interpreted to represent the results of the same geomorphic processes that create distinctively colored scarps, but with coloration suppressed by a thin lag or somewhat higher lithic content. (A: HiRISE image ESP_057901_1235 (56.2 °S, 103.1 °E), acquired at L_S=299°. B: HiRISE image ESP_052529_2345 (54.1 °N, 212.1 °E), acquired at L_S=72°. Illumination is from the upper (A) and lower (B) left.)
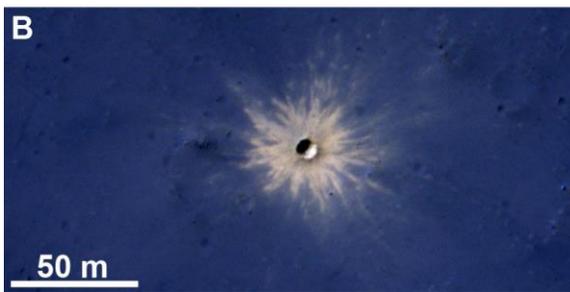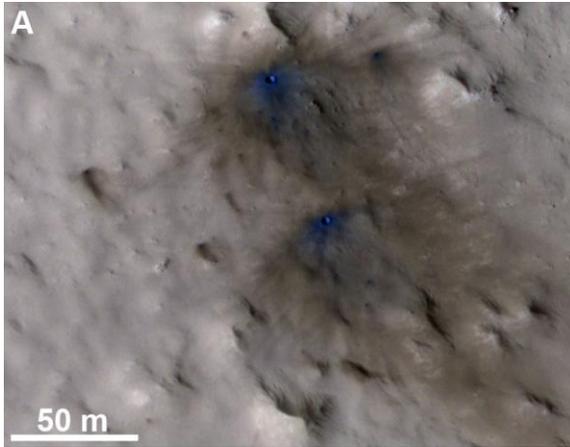
Figure 3. Examples of new craters with distinctive ejecta that are *not* interpreted as ice indicators. A) Cluster of craters with relatively blue ejecta that is not notably bright or distinctive; this coloration is consistent with mafic material exposed by the impact. B) Crater with relatively bright ejecta. This material appears relatively yellow (bright in the HiRISE red filter) rather than blue or white, and all excavated material appears bright even though any ice present at this latitude should lie beneath a debris cover. In neither case is nearby geomorphology suggestive of ice-rich material, and these latitudes do not theoretically favor shallow stable ice. (A: HiRISE image ESP_055383_2135 (33.2 °N, 58.1 °E), acquired at L_S=179°. B: HiRISE image ESP_044875_1650 (14.7 °S, 30.9 °E), acquired at L_S=112°. Illumination is from the lower (A) and upper (B) left.)
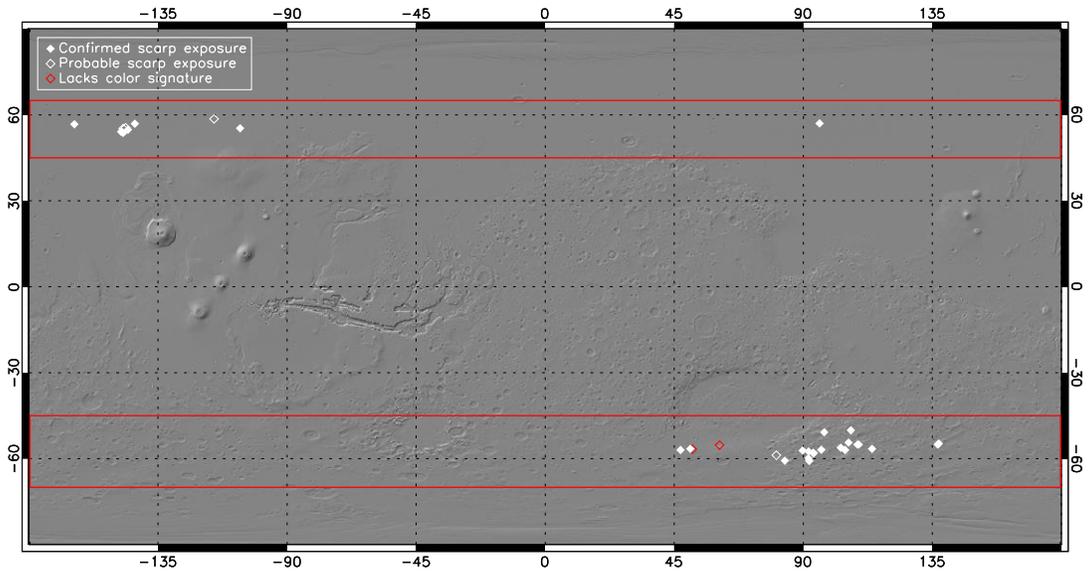
1498

Figure 4. Map of ice-exposing scarp locations identified between 45–70 °S and 45–65
°N. Confirmed scarps (relatively blue in HiRISE) are shown as solid symbols and
probable scarps are open. Some symbols overlap. Red boxes outline the survey areas.
Base map is shaded relief derived from the Mars Orbiter Laser Altimeter (MOLA) digital
elevation model in simple cylindrical projection.
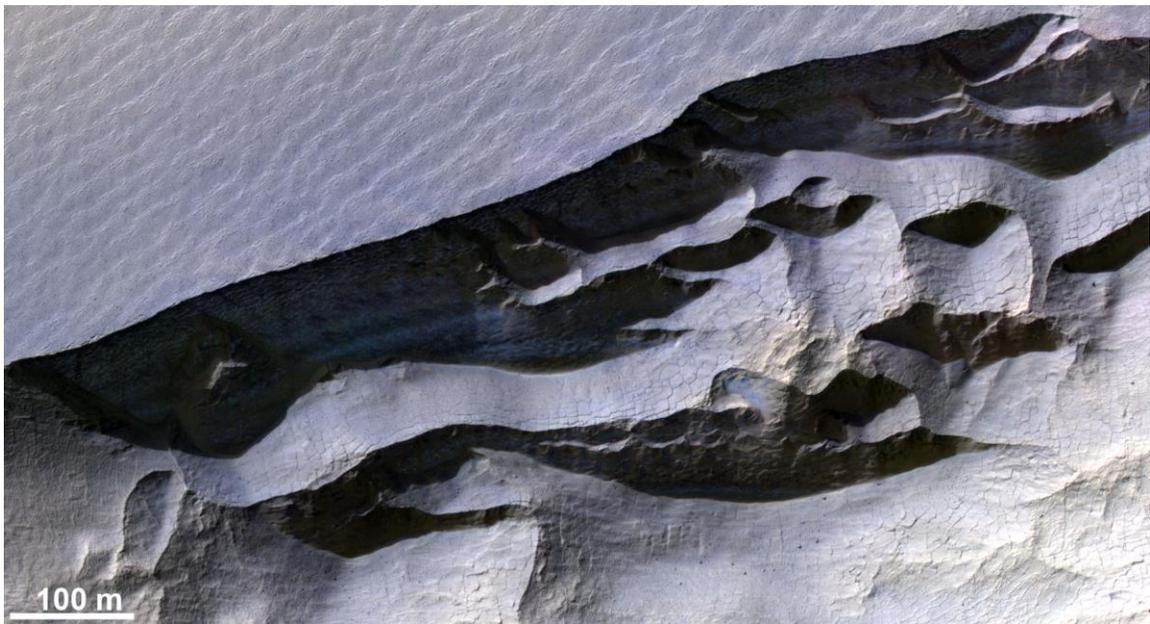
1504

1505 **Figure 5.** Southern-hemisphere scarp #15 (56.6 °S, 50.6 °E) has a complex structure. The

1506 primary scarp face and best ice exposure is largely in shadow. However, small parallel

1507 facets exist within the material at the base of the scarp. This demonstrates a high ice

1508 content within the residual material (the scarp did not erode to the base of the ice) and

1509 complex dynamics of reactivation. (HiRISE image ESP_058971_1230, acquired at

1510 L_S=346°. Illumination is from the upper left.)
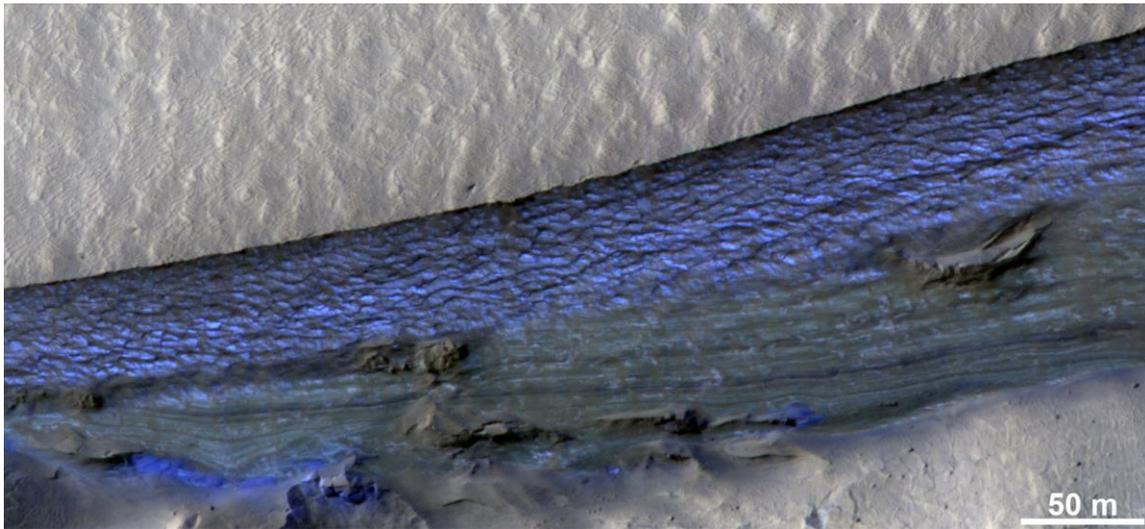
1511

1512 **Figure 6.** Contrasting layering styles in southern-hemisphere scarp #7 (57.5 °S, 91.9 °E).

1513 The lower slope (bottom of the image) shows a rare example of fine layering. The upper

1514 slope has a blocky and fractured appearance with some hints of horizontal banding,

1515 which is the typical appearance of most scarps. (HiRISE image ESP_057321_1220,

1516 acquired at L_S=272°. Illumination is from the upper left.)
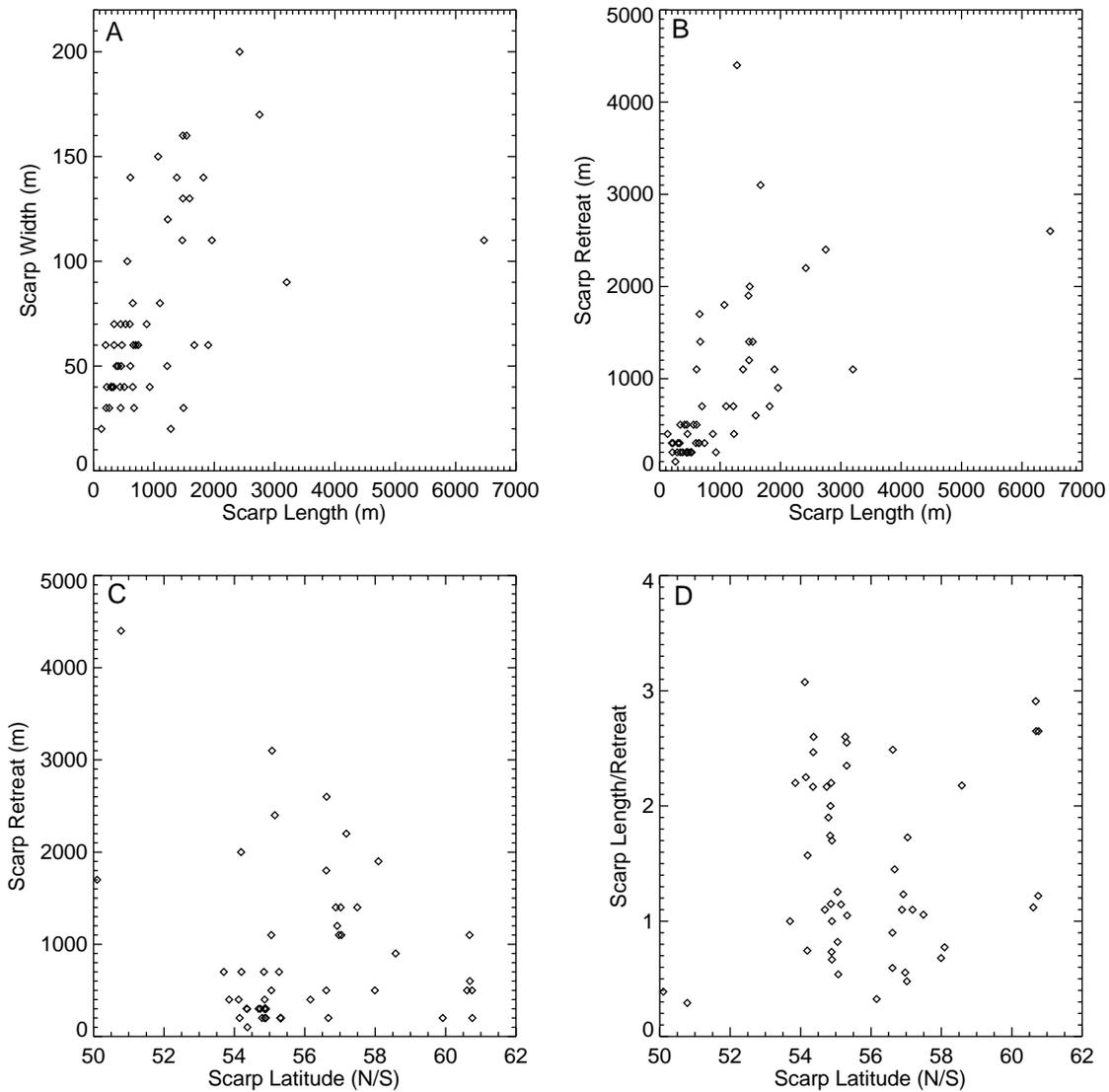
1517

Figure 7. Quantitative morphometry of ice-exposing scarps. A) Scarp plan-view width

(crest to base) versus end-to-end length. B) Scarp retreat distance versus end-to-end

length. Both A and B show that wider scarps are generally taller and have retreated

further. C) Scarp retreat distance versus latitude. The upper envelope of retreat distance

decreases with increasing latitude. D) Pit aspect ratio (scarp length divided by retreat

distance) versus latitude. All plots include data for confirmed scarps in both hemispheres.
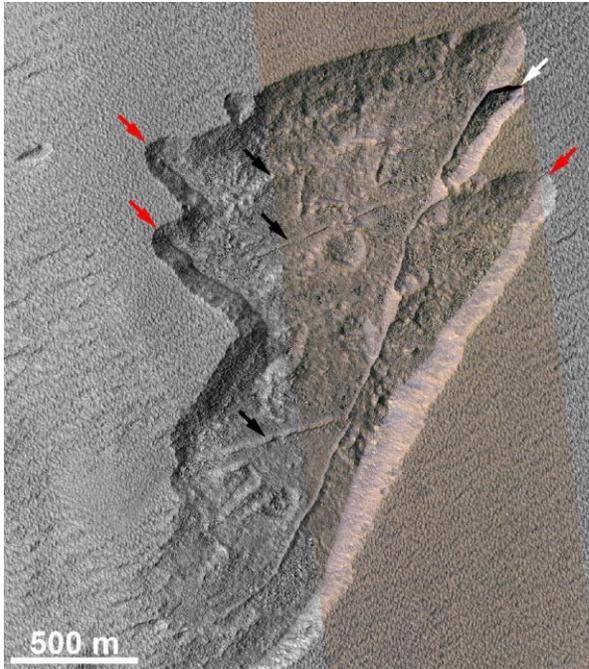
1524

1525 **Figure 8.** The pit containing southern-hemisphere scarp #13 (white arrow; see Fig. 2a for

1526 detail) reveals details of the scarp retreat process. Based on crosscutting relationships and

1527 the typical scarp geometry, the scarp initiated in the lower left part of the image and

1528 retreated approximately equatorward. It maintained the same approximate orientation

1529 throughout, as shown by several scarp-parallel ridges (black arrows). However, retreat

1530 may have been oblique rather than scarp-normal at times, since the scarp walls in the

1531 southern part of the pit are parallel but are not normal to the scarp. Multiple notches in

1532 the pit walls (red arrows) demonstrate that the scarp width varied over time and that the

1533 outer parts sometimes became inactive. It is possible that the entire scarp deactivated and

1534 only the central sections subsequently resumed retreating. Finally, secondary scarps such

1535 as the current scarp reactivated on the east side of the pit, producing a younger ridge that

1536 defines the old edge of the pit. (HiRISE image ESP_057901_1235 (56.2 °S, 103.1 °E),

1537 acquired at L_S=299°. Illumination is from the upper left.)
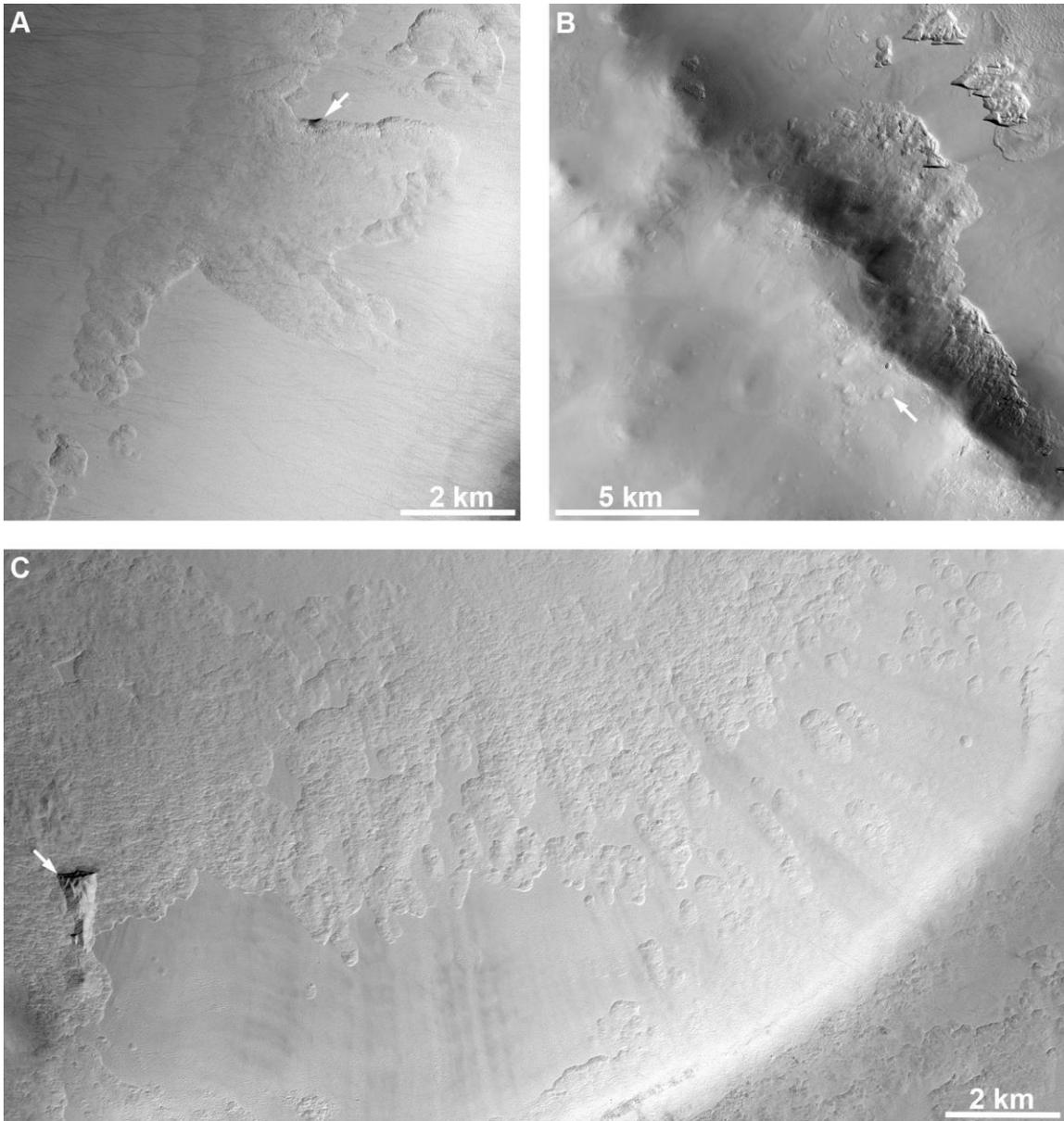
Figure 9. Scalloped depressions and ice-loss landforms. A) Probable ice-exposing

southern-hemisphere scarp #18 (arrow; 58.8 °S, 80.6 °E) eroding into a mantling unit that

is also being removed to form scalloped depressions. The scarp resembles parts of the

scalloped depressions but is the most-shadowed (steepest) slope in the area. B) A group

of scarps in southwestern Milankovič crater (54 °N, 212 °E) with expanded craters

nearby (arrow indicates a prominent example). Although both occur in mantling

1545   materials, the scarps are concentrated inside the crater rim and the craters beyond it. C)

1546   Southern-hemisphere ice-exposing scarp #14 (arrow) occurs in the vicinity of classic

1547   scalloped depressions prominent in the eastern part of the image (57 °S, 47.2 °E). The

1548   well-defined scallops are within a pristine mantling unit while the scarp is cut into

1549   partially degraded material that may have been previously dissected by scallop formation.

1550   Note that the triangular scarp-pit morphology is distinct from the scalloped depressions in

1551   shape and scale. (A: CTX image B10_013661_1211_XN_58S279W. Illumination is from

1552   the upper left. B: CTX image J22_053320_2345_XN_54N148W. Illumination from the

1553   lower left. C: CTX image K11_057692_1221_XN_57S312W. Illumination is from the

1554   upper left.)

1555
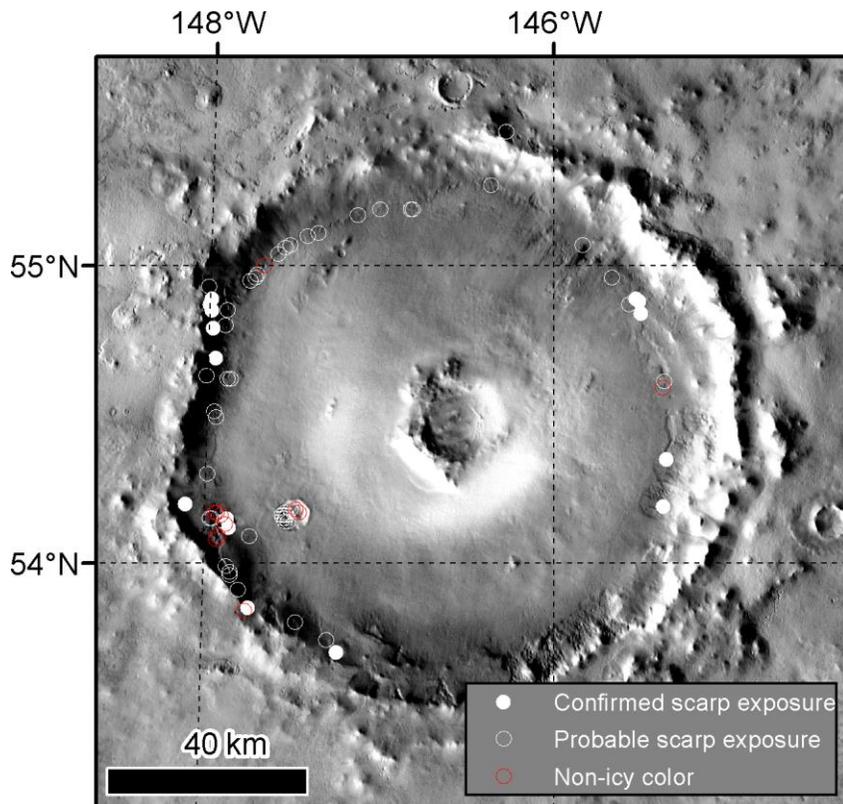
1556

1557 **Figure 10.** Map of scarps in Milankovič crater. Solid white circles show confirmed icy

1558 scarps, open white circles are classified as probable, and red symbols have the

1559 morphology of icy scarps but lack the coloration in HiRISE images. Scarps generally line

1560 the base of the crater rim, apart from a cluster in a smaller crater within Milankovič. Base

1561 map is the THEMIS controlled mosaic in sinusoidal projection centered on 146 °W.
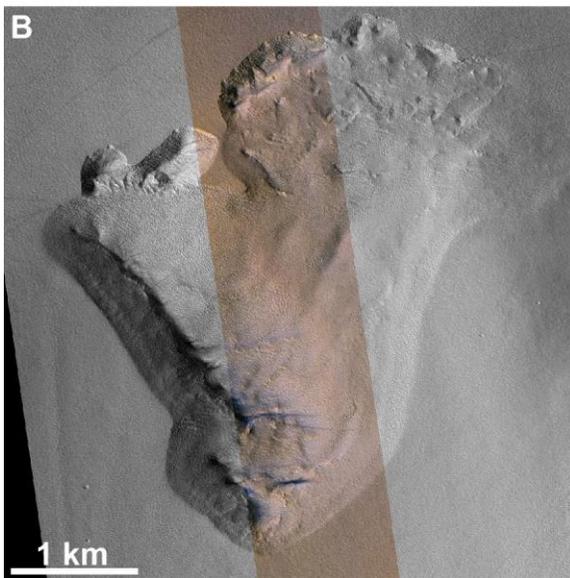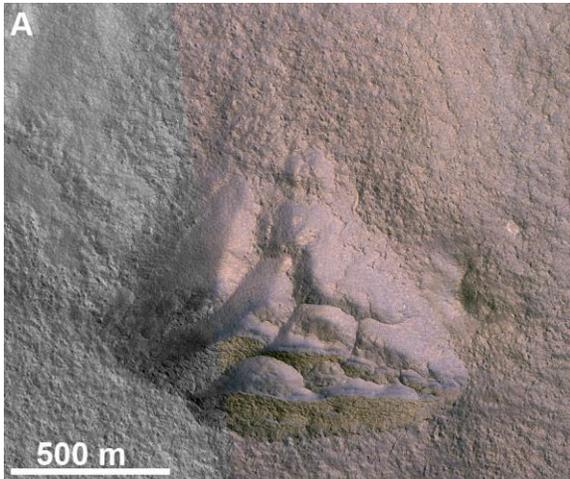
1562

1563 **Figure 11.** Pits with morphologies similar to ice-exposing scarp locations, but without

1564 well-defined scarps or distinct relatively blue exposures. (A: HiRISE image

1565 ESP_061998_2405 (60.4 °N, 197.8 °E), acquired at L_S=95°. B: HiRISE image

1566   ESP_057176_1255 (54 °S, 90.2 °E), acquired at L_S=265°. Illumination is from the left in

1567   both panels.)
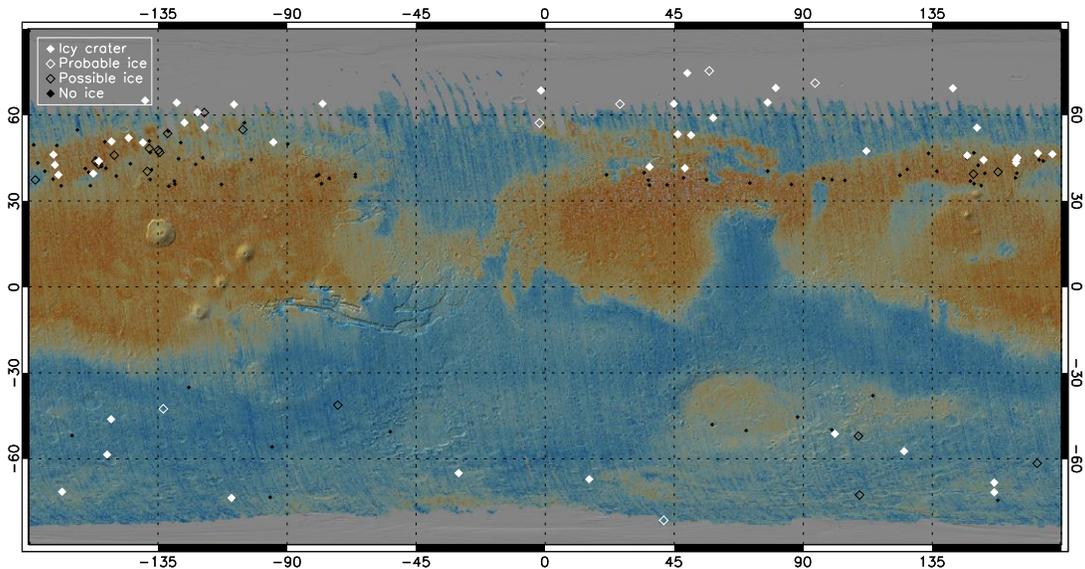
1568

Figure 12. Map of confirmed and probable ice-exposing craters (solid and open white

diamonds respectively), possible ice-exposing craters (open black diamonds), and non-

ice-exposing craters (black points) poleward of 35° latitude in each hemisphere. New

dated impacts equatorward of 35 °N/S are not shown in this figure. The background map

is the dust-cover index map of Ruff and Christensen (2002) in simple cylindrical

projection; new impact detections overall are biased towards dusty regions (orange and

yellow tones) although bright ice exposure might aid crater detection in non-dusty

regions.
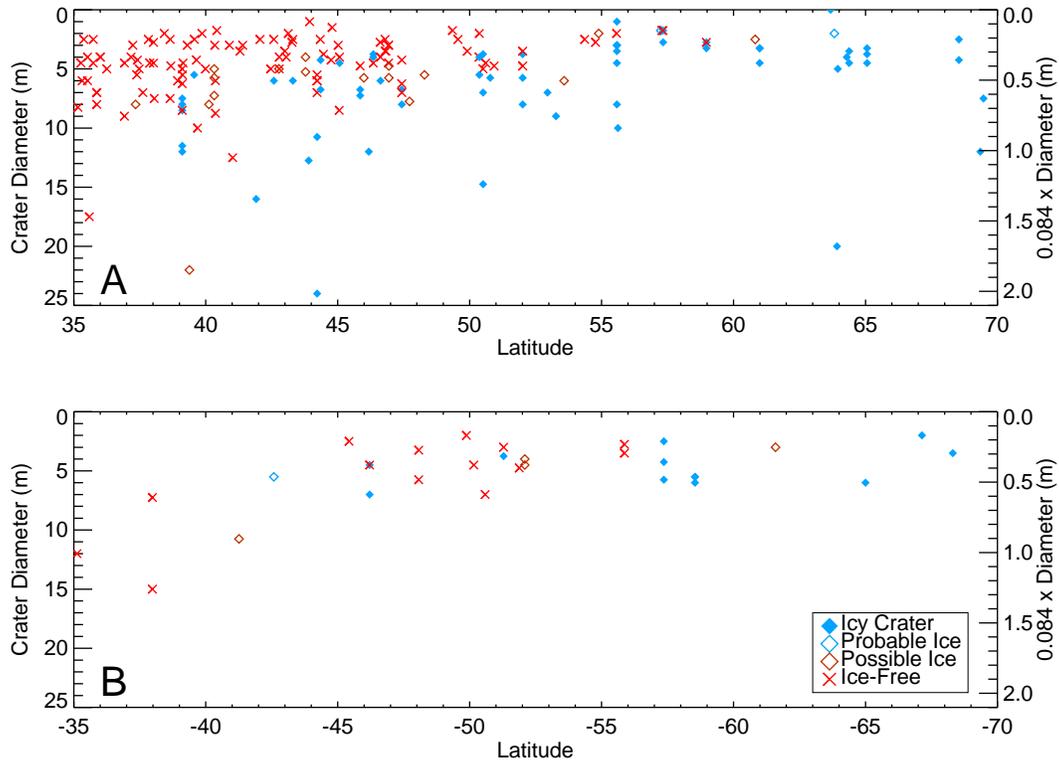
1577

Figure 13. Plot of latitude vs. crater diameter for new impacts in the northern hemisphere
(A) and southern hemisphere (B). Probable and confirmed ice-exposing craters are shown
in blue. The right-hand axis shows 0.084× the crater diameter, an estimate of the
maximum excavation depth. Some craters are at latitudes or diameters larger than the
maximum plotted but are excluded to enhance visibility of the shallow craters and
transitional latitudes. In both hemispheres the depth to ice becomes shallower at high
latitude, but at latitudes where ice exists it is commonly present at a depth <1 m,
consistent with ice stability theory.

1586

Figure 14. Ice-exposing craters in the Protonilus Mensae region. Both craters excavate

blocky ice-rich material. On the east (west-facing) crater wall, ice appears to be within

the core of a ridge (arrow). (A: HiRISE image ESP_046707_2220 (41.4 °N, 48.8 °E),

acquired at L_S=185°. B: HiRISE image ESP_046747_2220 (41.9 °N, 36.4 °E), acquired

at L_S=187°. Illumination is from the lower left in both panels.)
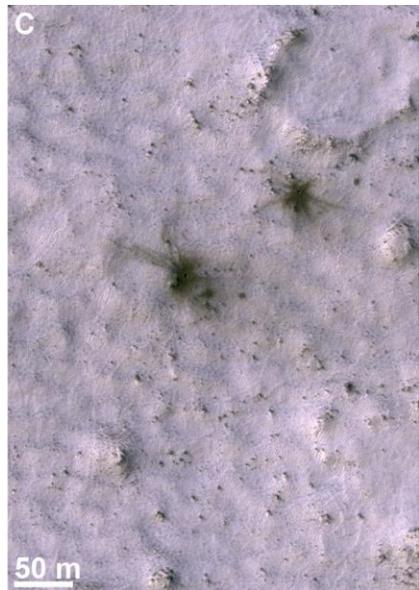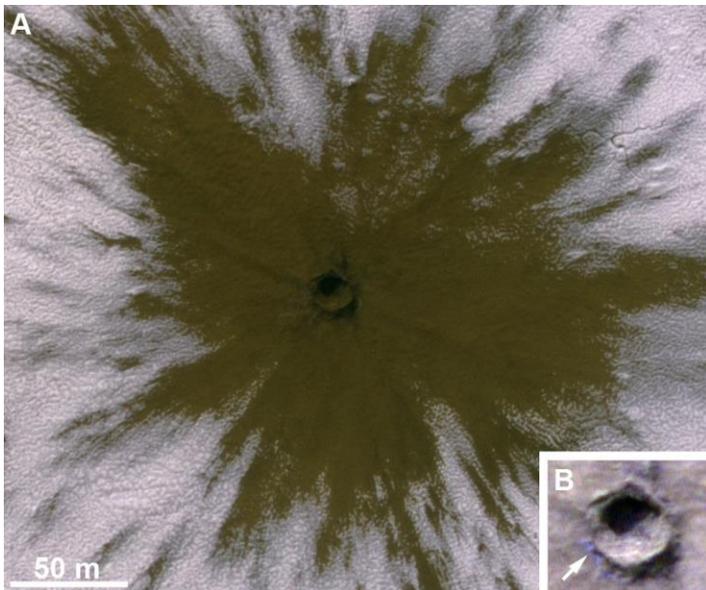
1592

1593 **Figure 15.** New impact craters with ejecta superposing seasonal frost. A) Crater on the

1594 south polar layered deposits (81.5 °S, 41.4 °E). B) The same crater (2× enlarged) after

1595 defrosting. Arrow indicates a minor exposure of relatively-blue material interpreted as

1596 probable ground ice; however, despite the ice-rich nature of the SPLD and substantial

1597 size of this crater, the distinct ice deposit is minimal even though images were acquired

1598 rapidly after formation. Note that the color stretch in this cutout is different from that in

1599 A, to emphasize relative color variations; the crater and immediate surroundings are

1600 unchanged but there is no longer frost providing a strong relative contrast. C) Small

1601 craters with ejecta superposing the seasonal CO_2 cap (55.9 °S, 264.8 °E). (A: HiRISE

1602 image ESP_057152_0985 (L_S=263°). North is towards upper right (polar stereographic

1603 projection) and illumination from the top. B: HiRISE image ESP_057574_0985

1604 (L_S=284°). C: HiRISE image ESP_037284_1240 (L_S=159°). North is up and illumination

1605 from the upper left.)

50 m   100 m
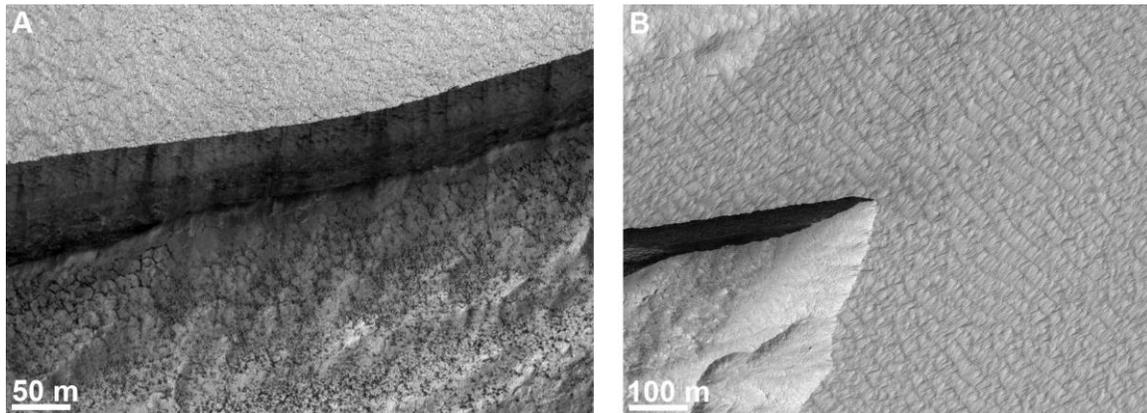
1606

1607 **Figure 16.** Possible modification processes maintaining ice exposures. A) Striations on

1608 the surface of a scarp with likely winter frost cover suggest active frost-driven mass

1609 wasting. B) Ridges on the plateau surface above southern-hemisphere scarp #3 resemble

1610 bedforms interpreted as dust accumulation features by Geissler (2014) and indicate winds

1611   from the upper right. (A: HiRISE image ESP_064006_1245 (55.1 °S, 109.4 °E), acquired

1612   at L_S=171°. B: HiRISE image ESP_040772_1215 (58.1 °S, 93.7 °E), acquired at

1613 L_S=322°. Illumination is from the upper left in both panels.)

1614